

Yuanquan Wang, Yuwei Wu, Yunde Jia

# Segmentation of the left ventricle in cardiac cine MRI using a shape-constrained snake model

March 6, 2013

Springer

**Abstract** Segmentation of the left ventricle (LV) is a hot topic in cardiac magnetic resonance (MR) images analysis. In this chapter, we introduce an automatic LV myocardial boundary segmentation method using the parametric active contour model (or snake model). By convolving the gradient map with the user-defined kernel function, a fast external force named gradient vector convolution (GVC) is presented for the snake model. A circle-based energy is incorporated into the GVC snake model to extract the endocardium. With this prior constraint, the snake contour can conquer the unexpected local minimum stemming from artifacts and papillary muscle, etc. After the endocardium is detected, two novel approach is developed to generate the desired edge map. These modified edge map are used to generate a new GVC force field, which automatically pushes the snake contour directly to the epicardium by employing the endocardium result as initialization. Meanwhile, a novel shape-similarity based energy is proposed to prevent the snake contour from being strapped in faulty edges and to preserve weak boundaries. Both qualitative and quantitative evaluations on our dataset and the publicly available database (e.g. *MICCAI 2009*) demonstrate the good performance of our algorithm.

**Key words:** Left ventricle segmentation, Cardiac MRI, Active contour model, Gradient vector convolution, Shape constraint.

## 0.1 Introduction

Cardiac magnetic resonance imaging has proven to be a versatile and noninvasive imaging modality. It can acquire the anatomical and functional information of a heart within a short period of time, and thus be widely used in clinical diagnosis [1]. The segmentation of cardiac magnetic resonance images (MRI) is one of the most critical prerequisites for quantitative study of the left ventricle (LV). Many clinically established diagnosis indexes such as wall thickness and ejection fraction are evaluated by the segmentation results of the LV.

In clinical practice, the LV segmentation task is often performed manually by an experienced clinician. The manual segmentation, however, is tedious, time consuming, subjective and irreproducible. Although an impressive research effort has been devoted to automatic LV segmentation, it remains a challenging problem, mainly because of the difficulties inherent from MR cardiac images [2]. For instance, since papillary muscles and the myocardium are connected, it is prone to take the papillary muscles as a part of the myocardium. Furthermore, the myocardium and neighbor organs such as the liver have almost the same intensity profile, leading to low contrast between them. In addition, a major difficulty in segmentation of the cardiac MR images is the intensity inhomogeneity due to the radio-frequency coils or acquisition sequences. There have been extensive researches such as graph cuts [3, 4], morphological operations [5, 6], dynamic weights fuzzy connectedness framework [7, 8], active contours or snake model [9, 10, 11, 12, 13, 2] and supervised learning

methods [14, 15, 16, 17], to overcome challenges of the LV segmentation. Petitjean and Dacher [18] presented a comprehensive review of LV segmentation algorithms.

Among approaches mentioned above, the snake model proposed by Kass *et al.* [9] is one of the most successful methods. It integrates an initial estimate, geometrical properties of the contour, image data and knowledge-based constraints into a single process, and provides a good solution to shape recovery of objects of interest in visual data. A traditional active contour model represented by a curve  $C(s) = (x(s), y(s))$ ,  $s \in [0, 1]$  moves through the spatial domain of an image to minimize the energy functional

$$E(C) = \int_0^1 \underbrace{\frac{1}{2} (\alpha |C'(s)|^2 + \beta |C''(s)|^2)}_{\text{Internal energy}} + \underbrace{g(C(s))}_{\text{External energy}} ds, \quad (0.1)$$

where  $C'(s)$  and  $C''(s)$  denote the first and second derivatives of  $C$  with respect to  $s$ , respectively. The first term of the integral stands for the internal force that keeps the contour continuous and smooth during deformation, the second term is the external force that drives the contour toward an object boundary or the other desired features within an image. By using the calculus of variation, the Euler equation to minimize  $E(C)$  is

$$\alpha C''(s) - \beta C'''(s) - \nabla g(C(s)) = 0. \quad (0.2)$$

In terms of representation and implementation, active contour models are classified into two categories: the parametric active contour models [19, 20, 21, 22, 23] and the geometric active contour models [24, 25, 26, 27]. In this chapter, we focus on the parametric active contour models, and our approach can be also integrated into geometric active contour models. Since the external force plays a leading role in driving the active contours to approach objects boundaries in the parametric active contour models, designing a novel external force field has been extensively studied [19, 21, 28, 29, 30, 31]. Among all these external forces, gradient vector flow (GVF) proposed by Xu and Prince [21], has been one of the most successful external forces, which is computed as a diffusion of the gradient vectors of a gray-level or binary edge map derived from a given image, and allowed to increase the capture range. Due to the outstanding properties of GVF, a large number of modified versions have been presented [32, 28, 30, 33] to improve the performance of active contour models. However, researchers found that the GVF suffers from several challenges including narrow and deep concavity convergence as well as weak edge leakage.

In this chapter, a convolution-based external force called gradient vector convolution (GVC) is introduced. The GVC method is motivated by gradient vector flow (GVF) and possesses some advantages of the GVF such as enlarged capture range, initialization insensitivity, concavity convergence, but its computational cost is low owing to its convolution mechanism. Some experiments are presented to demonstrate these advantages.

### 0.1.1 Active contour model based LV segmentation without prior

The studies regarding the LV segmentation using active contour models have mainly concentrated on the design of the *external energy* term. Ranganath [34] tracked the LV endocardium in cardiac MRI sequences by propagating the conventional snake from one frame to another. Makowski *et al.* [35] employed the balloon snake [19] to extract the LV endocardium and introduced an antitangling strategy to exclude the papillary muscles. The balloon force is defined as

$$\mathbf{F} = k_1 \overrightarrow{\mathbf{n}(s)} - k_2 \frac{\nabla E_{image}}{\|\nabla E_{image}\|}, \quad (0.3)$$

where  $\overrightarrow{\mathbf{n}(s)}$  is the normal unit vector to the curve at point  $C(s)$  and  $k_1$  is the amplitude of the force. If we change the sign of  $k_1$  or the orientation of the curve, it will have an effect of deflation instead of inflation. The curve expands and it is attracted and stopped by edges as before, but since there is a pressure force, if the edge is too weak the curve can pass through this edge. Therefore, it is prone to lead to weak edge leakage during LV segmentation. Based on the discrete contour model, Hautvast *et al.* [36] developed a method that attempts to maintain a constant contour environment in the vicinity of the cavity boundary. Due to the high performance of capture range enlarging, Santarelli *et al.* [37] employed the gradient vector flow (GVF) snake [21] for the LV segmentation [37], but did not consider the effect of weak boundaries, papillary muscle and artifacts stemming from swirling blood. It is also not clear how the GVF snake model captured the epicardium soon after the endocardium was extracted. Lee *et al.* [38] presented the iterative thresholding method to extract the endocardium, which effectively alleviates the interference of papillary muscle. However, the endocardial contour is not smooth enough and the movement constraint based on image intensity for the snake is too empirical. Nguyen *et al.* [39] compared the conventional snake, balloon snake and GVF snake on extracting the LV endocardium and concluded that the GVF snake has the best performance.

However, the information (e.g. intensity, texture) only deriving from the image itself is not sufficient to get satisfactory segmentation results of the LV. It is difficult to deal with the noisy and incomplete data. The prior knowledge concerning the LV, therefore, is necessary to be incorporated into the snake model. The prior information may be the statistical shape from a training set [10, 40, 41], be anatomical information such as an ellipse [42, 43, 44], or be intensity statistics [45, 46, 47].

### 0.1.2 Active contour model based LV segmentation with weak prior

Lynch *et al.* [46] presented a novel and intuitive approach to combine 3-D spatial and temporal MRI data in an integrated segmentation algorithm to extract the myocardium of the left ventricle. By encoding prior knowledge about cardiac temporal evolution, an EM algorithm optimally tracks the myocardial deformation over the

cardiac cycle. Punithakumar *et al.* [47] presented an original information theoretic measure of heart motion based on the Shannon's differential entropy (SDE), which allows heart wall motion abnormality detection. Folkesson *et al.* [41] presented a segmentation method that extends the geodesic active region method by the incorporation of a statistical classifier trained using feature selection. Paragios [40] integrated visual information with anatomical constraint into the variational level set approach [48]. The combination of visual information and anatomical constraints can achieve the geometric flow for the LV segmentation expressed as

$$\begin{aligned} \frac{d}{dt} \partial \mathcal{R}(u) &= \gamma \left[ \underbrace{C(d(\partial \mathcal{R}_I(u), \partial \mathcal{R}_0)))}_{\text{anatomical constraint}} \right] \mathcal{N}(u) + \left[ \underbrace{\beta [r(p(I(u))) - r(p_0(I(u)))]}_{\text{region homogeneity}} \right. \\ &\quad \left. + \epsilon g(|\nabla I(u)|) [(1-\alpha)K(u) + \alpha(\tilde{v}(u) \cdot \mathcal{N}(u))] \right] \mathcal{N}(u) \\ \frac{d}{dt} \partial \mathcal{R}_0(u) &= = \gamma \left[ C_0(d(\partial \mathcal{R}_I, \partial \mathcal{R}_0(u))) \right] \mathcal{N}(u) + \left[ \beta [r(p_0(I(u))) - r(p_B(I(u)))] \right. \\ &\quad \left. + \epsilon g(|\nabla I(u)|) [(1-\alpha)K_0(u) + \alpha(\tilde{v}(u) \cdot \mathcal{N}_0(u))] \right] \mathcal{N}_0(u). \end{aligned} \quad (0.4)$$

Ayed *et al.* [11] proposed to get curve evolution equations by minimizing two functionals each containing an original overlap prior constraint between the intensity distributions of the cavity and myocardium. For each region  $\mathbf{R} \in \{C^n, M^n, B^n, n = 1, 2, \dots, N\}$ , define  $P_{\mathbf{R}, I}$  as the nonparametric (kernel-based) estimate of intensity distribution within region  $\mathbf{R}$  in frame  $I \in \{I^n, n = 1, 2, \dots, N\}$

$$\forall z \in \mathbb{R}^+, P_{\mathbf{R}, I}(z) = \frac{\int_{\mathbf{R}} K(z - I(\mathbf{X})) d\mathbf{X}}{a_{\mathbf{R}}}, \quad (0.5)$$

where  $a_{\mathbf{R}}$  is the area of region  $\mathbf{R}$

$$a_{\mathbf{R}} = \int_{\mathbf{R}} d\mathbf{X}. \quad (0.6)$$

Ayed *et al.* [11] assume that a segmentation of the first frame  $I^1$ , i.e., a partition  $\{C^1, M^1, B^1\}$  is given. consider

$$\mathbf{B}_{in}^n = \mathcal{B}(P_{C^n, I^n} / P_{M^1, I^1}). \quad (0.7)$$

$\mathbf{B}_{in}^n$  measures the amount of overlap between the intensity distribution within the heart cavity region in  $I^n$  and the myocardium model learned from the first frame. Similarly, the background model learned from the first frame is given by

$$\mathbf{B}_{out}^n = \mathcal{B}(P_{M^n, I^n} / P_{B^1, I^1}). \quad (0.8)$$

Mean-matching terms measures the conformity of intensity means within the cavity and the myocardium in the current frame to mean priors learned from the first frame

$$\begin{cases} \mathcal{M}_{in}^n = (\mu_{in}^n - \mu_{in}^1)^2 \\ \mathcal{M}_{out}^n = (\mu_{out}^n - \mu_{out}^1)^2 \end{cases}, \quad (0.9)$$

where

$$\begin{cases} \mu_{in}^n = \frac{\int_{C^n} I^n d\mathbf{X}}{a_{C^n}} \\ \mu_{out}^n = \frac{\int_{M^n} I^n d\mathbf{X}}{a_{M^n}} \end{cases}.$$

The gradient terms is defined as

$$\begin{cases} \mathcal{G}_{in}^n = \oint_{\vec{\Gamma}_{in}^n} (g_n + c) ds \\ \mathcal{G}_{out}^n = \oint_{\vec{\Gamma}_{out}^n} (g_n + c) ds \end{cases},$$

where  $c$  is a positive constant and  $g_n$  is an edge indicator. The functionals to minimize are a weighted sum of the three characteristic terms (i.e., overlap prior terms, mean-matching terms and gradient terms)

$$\begin{aligned} \mathcal{F}_{in}^n &= \alpha \mathcal{O}_{in}^n + \beta \mathcal{M}_{in}^n + \lambda \mathcal{G}_{in}^n \\ &= \alpha (\mathbf{B}_{in}^n - \mathbf{B}_{in}^1)^2 + \beta (\mu_{in}^n - \mu_{in}^1)^2 + \lambda \oint_{\vec{\Gamma}_{in}^n} (g_n + c) ds \\ \mathcal{F}_{out}^n &= \alpha \mathcal{O}_{out}^n + \beta \mathcal{M}_{out}^n + \lambda \mathcal{G}_{out}^n \\ &= \alpha (\mathbf{B}_{out}^n - \mathbf{B}_{out}^1)^2 + \beta (\mu_{out}^n - \mu_{out}^1)^2 + \lambda \oint_{\vec{\Gamma}_{out}^n} (g_n + c) ds. \end{aligned} \quad (0.10)$$

Although excellent results have been achieved in [40, 41, 11] where the LV shape is learned from an annotated training data set, the segmentation performance depends heavily on the size and richness of images in the training set.

To relax the dependence on the choice of a training set, Zhu *et al.* [49] built a subject-specific dynamic model from a user-provided segmentation of one frame in the current cardiac sequence, which is able to simultaneously handle temporal dynamics (intrasubject variability) and intersubject variability. The Bayesian framework combining the forward and backward segmentation is expressed as

$$\begin{aligned}
\hat{\mathbf{s}}_t &= \arg \max_{\mathbf{s}_t} P(\mathbf{s}_t | I_{1:N}) \\
&= \arg \max_{\mathbf{s}_t} P(I_t | \mathbf{s}_t) P(\mathbf{s}_t | \hat{\mathbf{s}}_{1:t-1}^+) P(\mathbf{s}_t | \hat{\mathbf{s}}_{t+1:N}^-) \\
&= \arg \max_{\mathbf{s}_t} \left\{ \underbrace{\log P(I_t | \mathbf{s}_t)}_{\text{data adherence}} + \underbrace{\log P(\mathbf{s}_t | \hat{\mathbf{s}}_{1:t-1}^+)}_{\text{forward dynamics}} + \underbrace{\log P(\mathbf{s}_t | \hat{\mathbf{s}}_{t+1:N}^-)}_{\text{backward dynamics}} \right\}
\end{aligned} \tag{0.11}$$

Ayed *et al.* [2] introduced a novel max-flow segmentation of the LV by recovering subject-specific distributions learned from the first frame via a bound of the Bhattacharyya measure. The total cost function is given by

$$\begin{aligned}
\arg \min_{L:P \rightarrow 0,1} & \left[ - \sum_{i \in I} \sqrt{\mathbf{P}_{L,I^c}(i) \mathcal{M}_{c,I}(i)} - \sum_{d \in D} \sqrt{\mathbf{P}_{L,D^c}(d) \mathcal{M}_{c,D}(d)} \right. \\
& \left. + \sum_{\{p,q\} \in \mathcal{N}} \frac{1}{||p-q||} \delta_{L(p) \neq L(q)} \right],
\end{aligned} \tag{0.12}$$

where  $\mathcal{M}_{c,I}$  is the learned model distribution of intensity and  $\mathcal{M}_{c,D}$  is the model distribution of distances within the cavity in the learning frame. Jolly *et al.* [50] combined the edge, region and shape information to extract the LV endocardium, the approximate shape of the LV is obtained based on the maximum discrimination method. They used the shape alignment method proposed by Duta *et al.* [51] to establish the correspondence between a subset  $A'$  of the template points and a subset  $B'$  of the candidate points. The goal of shape constraint in [50] is to find the coefficients  $(a, b, c, d)$  of the similarity transform which minimize the distance  $f(N_c)$ .

$$\begin{aligned}
f(N_c) &= \frac{1}{N_c^2} \sum_{j=1}^{N_c} w(B_j) \left[ (x_{A_j} - ax_{B_j} - cy_{B_j} - b)^2 \right. \\
&\quad \left. + (y_{A_j} - ay_{B_j} - cx_{B_j} - d)^2 \right] + \frac{2}{N_c},
\end{aligned} \tag{0.13}$$

where  $N_c$  is the number of established correspondence.

### 0.1.3 Active contour model based LV segmentation with strong prior

As shown by the growing literature on the LV segmentation, it benefit from the use of an anatomical constraint (e.g., shape model) on active contour model to enhance the robustness and accuracy of the segmentation. Pluempiwiriyawej *et al.* [43] incorporated the ellipse constraint into the segmentation scheme. However, estimating the five parameters of the ellipse is an isolated step, which does not comply with the evolution of the snake contour. Liang *et al.* [13] proposed a radial gradient vector flow (RGVF) snake to segment LV automatically. In [13], the ROI could be trans-

formed into polar coordinates where myocardium looks more like a horizontal band rather than a circle. This shape characteristic enables snake to evolve towards 1D radial direction instead of 2D image plane, which simplifies snake energy functions to 1D.

The atlas warping technique introduced by Lorenzo-Valdés *et al.* [52] is a typical training-based method, the atlas is constructed from manually segmented and temporally aligned data and is registered on the data for automatic segmentation. The active shape model (ASM) first proposed by Cootes *et al.* [14] is constructed from a training set of segmented objects using the principal component analysis (PCA) algorithm. The active appearance model (AAM) is extended from the ASM by taking into account the intensity distribution in the training set [15]. The AAM is more robust than the ASM when the intensity contrast is low and the object boundary is weak. There has been a great diversity of works devoted to the construction and application of the ASM/AAM models, particularly for the extraction of the LV from cardiac MRI. Mitchell *et al.* [53] devised a multistage hybrid active appearance model (AAM) by combining ASM and AAM. Zambal *et al.* [54] combined AAM and ASM for the LV segmentation, in which the global model construction interconnects a set of 2D AAM by a 3D shape model. Recently, Zhang *et al.* [16] also combined the ASM and AAM but to construct a biventricular model to segment the left and right ventricles simultaneously.

#### **0.1.4 Overview of our method**

In this chapter, we adopt a novel LV segmentation method to address the following challenges: (1) image inhomogeneity; (2) effect of papillary muscle; and (3) lack of edge information. Different from the methods in [40, 41], we focus on achieving a novel method to delineate the LV boundaries using the anatomical shape of the LV, rather than using the constraints derived from a finite training set. Our strategy is based on the parametric snake model, in which the external force is gradient vector convolution (GVC). The GVC snake model possesses similar properties of the GVF snake model, and it can be implemented in real time due to its convolutional nature. Considering the LV is roughly a circle, a circle-shape based energy is integrated into the GVC snake model to extract the endocardium of the LV. Compared with the shape constraints employed in [43], the proposed method does not need to estimate the shape parameters explicitly. In terms of epicardium segmentation, supposing the epicardium resembles the endocardium in shape, we develop a shape-similarity energy functional to prevent the snake contour from leaking out from weak boundaries. With all these strategies, we can extract the endocardium and epicardium of the LV from MR images robustly and accurately. This method is an extension of our approaches presented in [55, 12, 56], with more complete literature review, methodology derivations and experiments (including a new comparison with *MICCAI 2009* database [57]). The proposed approach consists of the following steps as shown in Fig. 0.1:

- Automatic localization of the LV. Hough transform is applied to intensity difference image to locate the LV centroid and the ROI.
- Designing the external force for snake model. The external force field plays a leading role in driving the active contours to approach objects boundaries in the snake model, and thus significantly influences the segmentation performance. A novel external force called gradient vector convolution (GVC) is proposed. The GVC snake is of great capture range, and is much more robust toward detecting and preserving the weak edges.
- The endocardium segmentation. Considering that the LV is roughly a circle, a circle-shape based energy functional is integrated into the GVC snake model to extract the endocardium.
- The epicardium segmentation. We adopt the segmentation result of the endocardium as *a priori* shape and construct a new shape-similarity based energy for GVC snake model, to get an accurate estimate of the epicardium.
- Assessment of segmentation accuracy. The segmentation results are compared with the state-of-the-art methods using the mean absolute distance (MAD) and Dice metric (DM).

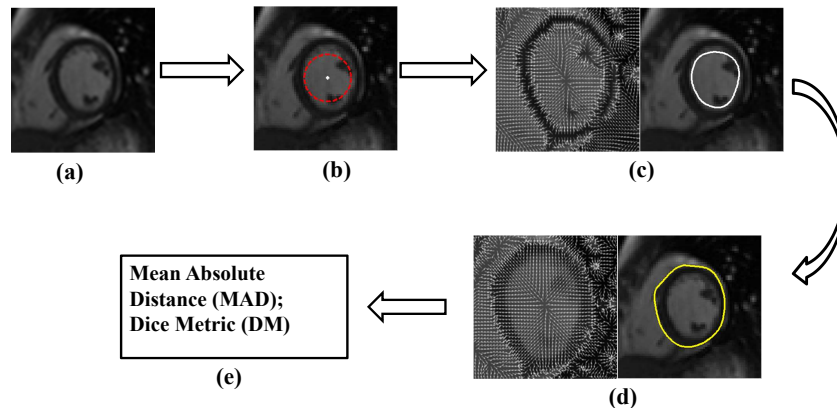


**Fig. 0.1** Framework for segmenting the cardiac cine MRI. (a) The cardiac cine MRI input; (b) Automatic localization of the LV; (c) The external force of snake model for segmenting endocardium and the segmentation result; (d) The external force of snake model for segmenting epicardium and the segmentation result; (e) Evaluation of segmentation results.

## 0.2 Gradient vector convolution for the snake model

### 0.2.1 GVF active contours

Notwithstanding the marvelous ability in representing object shapes, the traditional active contour model is limited to capture range and poor convergence to boundary concavities. Gradient vector flow (GVF) was proposed by Xu and Prince [21] as a new external force for active contour model to overcome these issues. It is a dense vector field, generated by diffusing the gradient vectors of a gray-level or binary edge map derived from an image. The GVF field is defined as a vector field  $\mathbf{V}(x,y) = [u(x,y), v(x,y)]$  that minimizes the following energy functional:

$$E(u,v) = \iint \left[ \mu (u_x^2 + u_y^2 + v_x^2 + v_y^2) + |\nabla f|^2 |\mathbf{V} - \nabla f|^2 \right] dx dy, \quad (0.14)$$

where  $f$  is the edge map defined as  $f(x,y) = |\nabla I(x,y)|$  or  $f(x,y) = |\nabla(G_\delta(x,y) \otimes I(x,y))|$  for gray level images.  $|\nabla f|$  is high near the edges and nearly zero in homogeneous regions and  $\mu$  is a positive weight to control the balance between smoothness energy and edge energy. We see that when  $|\nabla f|$  is small, the energy is dominated by sum of the squares of the partial derivatives of the vector field, yielding a slowly-varying field. On the other hand, when  $|\nabla f|$  is large, the second term dominates the integrand and minimized by setting  $\mathbf{V} = |\nabla f|$ . This produces the desired effect of keeping  $\mathbf{V}$  nearly equal to the gradient of the edge map when it is large, but forcing the field to be slow-varying when in homogeneous regions.

By the calculus of variation, the minimization of Eq. (0.14) reduces to solving the following Euler-Lagrange equation:

$$\mu \nabla^2 \mathbf{V} - (\mathbf{V} - \nabla f) (f_x^2 + f_y^2) = 0. \quad (0.15)$$

The equations evolving Eq. (0.15), embedded into a dynamic scheme by treating  $\mathbf{V}(x,y)$  as the function of  $t$ ,  $x$  and  $y$ , formally are

$$\begin{cases} \frac{\partial u}{\partial t} = \mu \cdot \underbrace{\nabla^2 u}_{\text{diffusion term}} - \underbrace{(u - f_x)(f_x^2 + f_y^2)}_{\text{data attraction term}} = 0 \\ \frac{\partial v}{\partial t} = \mu \cdot \underbrace{\nabla^2 v}_{\text{diffusion term}} - \underbrace{(v - f_y)(f_x^2 + f_y^2)}_{\text{data attraction term}} = 0, \end{cases} \quad (0.16)$$

where  $\nabla^2$  is the Laplacian operator. The active contour model with  $\mathbf{V}(x,y)$  as external force is called GVF active contour model.

### 0.2.2 Analysis of GVF active contour model

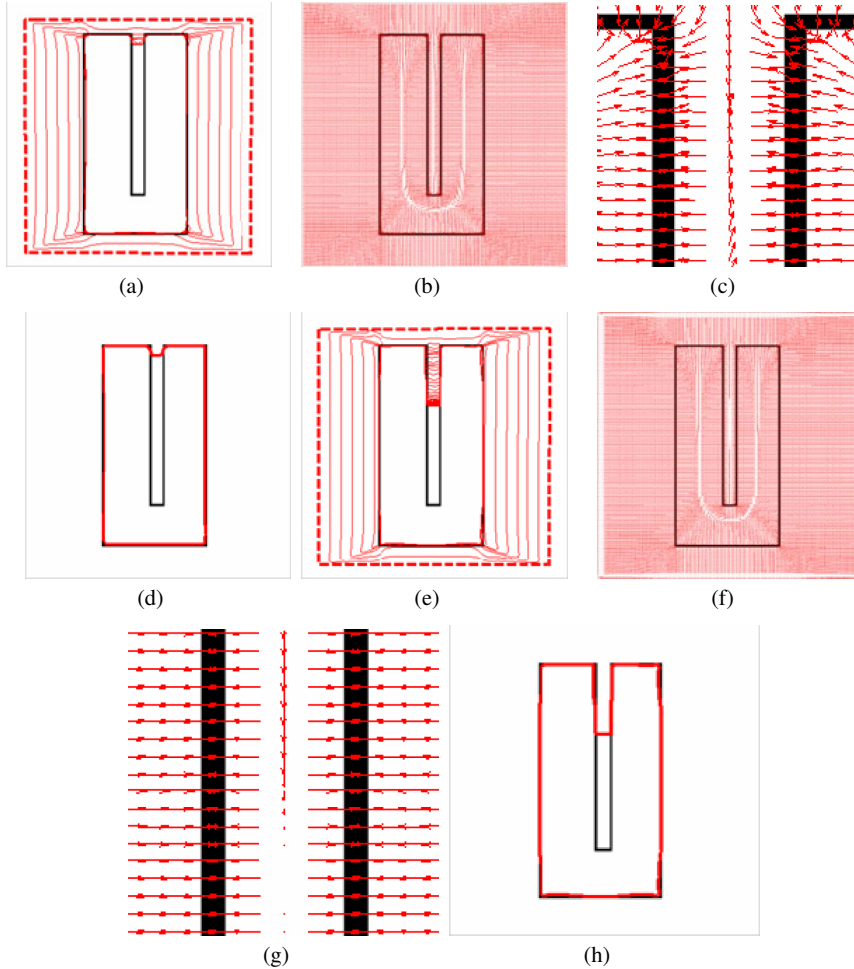


**Fig. 0.2** GVF and GGVF performance of narrow and deep concavity convergence. (a) GVF active contour model initialization and evolution; (b) GVF force field; (c) local close-up of (b); (d) GVF active contour model segmentation result; (e) GGVF active contour model initialization and evolution; (f) GGVF force field; (g) local close-up of (f); (h) GGVF active contour model segmentation result.

GVF has successfully addressed the issues of building a satisfactory capture range and approaching boundary concavities, e.g., U-shape concavity convergence. However the GVF active contour model still fails to converge to narrow and deep

concavity and would leak out around weak edges, especially neighbored by strong ones.

(a) *Narrow and deep concavity*: GVF can be regarded as a vector field constructed by diffusing original gradient vectors from near image edges to homogeneous regions, or from areas of non-zero vectors to ones of zero-vectors. The directions of vectors in the GVF field indicate the moving directions of Snaxels. The magnitudes of vectors take larger values near the image edges, and they decrease to zero as vectors goes away from image edges. This prevents the active contours moving into the long, thin boundary indentations. In addition, excessive smoothing of the field near the boundaries governed by the constant coefficient  $\mu$ , also results in the failure of narrow and deep concavities convergence.

This drawback of GVF can be seen from the example in Fig.0.2(a)-Fig.0.2(d). Fig.0.2(a) shows the GVF active contour model initialization and evolution of a synthetic image which is a concavity of 5-pixel width and 80-pixel depth. If we take a close-up to the GVF vector field in Fig.0.2(c), we can see the contradiction of forces from two opposite directions. This contradiction makes the temporary boundary stop moving. The segmentation result of GVF active contour model is shown in Fig.0.2(d).

A number of methods have been proposed to address this problem. Xu and Prince [32] introduced the generalized GVF (GGVF) active contour model to improve the original GVF by replacing the constant weighting coefficient  $\mu$  with two spatially varying weighting function. However, there is no essential difference between GGVF and GVF. The ability of entering into the concavity of edge is also limited. The illustration can be found in Fig.0.2(e)-Fig.0.2(h). Yu *et al.*[58] presented the normalized gradient vector diffusion by balancing the effect between weak vectors and strong vectors to improve the performance of GVF active contour model in deep concavity convergence. Hou *et al.* [59] proposed force field analysis active contour model, based on analyzing force distribution rules via Euclidean distance transformations. Similarly, Rodtook *et al.* [60] extended GGVF by introducing an adaptive edge map derived from continuous orientation force field analysis. Sum and Cheung [61] proposed the boundary vector field external force, under whcih the active contour evolves in two phases and moves into semi-closed concave region. Decomposing diffusion term in Eq.(0.16) as weighted sum of the two directional derivatives along normal and tangent direction, Ning *et al.* [62] exploited the normal gradient vector flow (NGVF) to ameliorate the concavities convergence by only adopting normal direction diffusion. However, it is unreasonable due to the fact that diffusion in tangent direction is inclined to smooth the noise while preserving edges. Wang *et al.* [63] further elaborated the mechanism of GVF from the perspective of Helmholtz decomposition, and introduced harmonic gradient vector flow (HGVF) which could converge to narrow concavities. Employing the measurement update energy term and separate prior energy term, Mishra *et al.* [29] demonstrated that the decoupled active contour model (DAC) can capture the regions of very high curvature and is robust to noise.

(b) *Weak edge leakage*: In GVF active contour model, at the location where a weak edge is very close to a strong one, the active contour readily leads to bound-

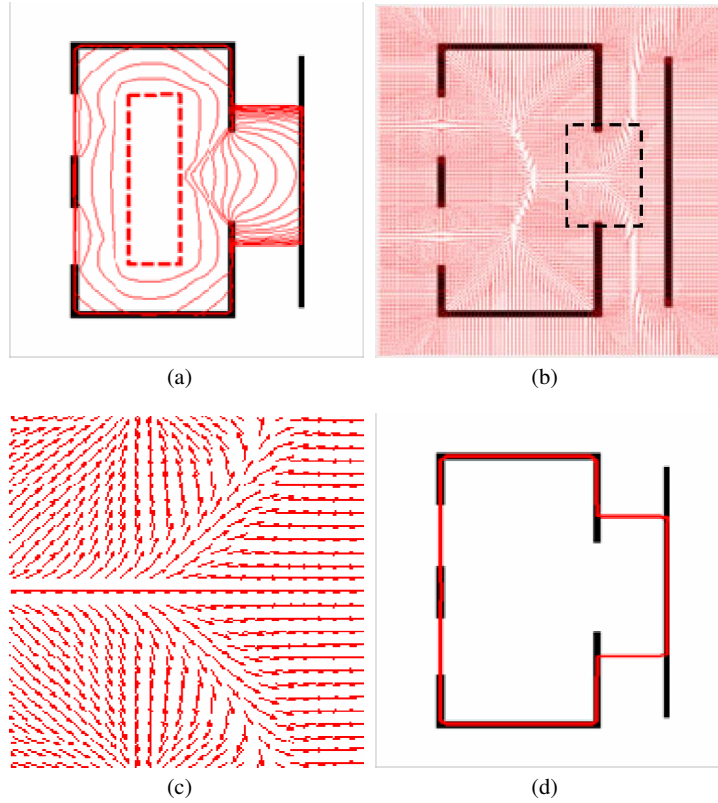


**Fig. 0.3** Weak edge leakage of GVF active contour model. (a) initialization and evolution; (b) GVF Force field; (c) close-up of the vector field inside the dashed rectangle of (b); (d) segmentation result.

aries leakage. This can be explained by the inherent competition of the diffusion process: It is well known that  $\nabla^2 u$  and  $\nabla^2 v$  are in the nature of very strong isotropic smoothing properties and cannot preserve edges in the diffusion term of Eq.(0.16), as  $t$  increases, the isotropic smoothing effect will dominate the diffusion. Moreover, the better force field highly depends on  $\mu$ . However, if  $\mu$  is too large, the active contours will tend to larger deviation from the original data and easily leak from weak edges. If  $\mu$  is small enough, this over-smoothing efficiency could be depressed, but, at the same time, the force field preserves excessive noise. This is a dilemma for GVF to suppress noise and preserve weak edge simultaneously

In Fig.0.3, we construct a particular image to show the performance of GVF active contour model at weak edge preserving. In this image, there is a gap neighbored by a strong line. Fig.0.3(b) shows that GVF force field, and the regions indicated by the dashed rectangle will be enlarged in Fig.0.3(c) such that the vector field can be more clearly displayed. The GVF active contour model is attached incorrectly toward to strong line in Fig.0.3(a) result from the GVF is difficult to prevent the

vectors near the boundary gap from being significantly influenced by the nearby strong one (see Fig.0.3(c)). The segmentation result is shown in Fig.0.3(d).

Recently some modified GVF active contour model have been developed to address this issue. Li *et al.* [64] proposed edge preserving gradient vector flow (EPGVF), which makes  $\mathbf{V}(x,y)$  projection along object edges to be better for preserving edges. Some improved results have been acquired by a robust region-based segmentation method introduced by Xie and Mirmehdi [65]. By generalizing the Laplacian operator from flat space to manifold during diffusion, Lu *et al.* [33] presented gradient vector flow over manifold (GVFOM) which outperforms GVF in terms of weak edge preserving, concavities convergence. Tang [28] exploited the multi-direction GVF active contour to trace the boundary of the skin cancer even if there are other objects near the skin cancer region. By integrating the gradient vector flow and the prior directional information, Zhu *et al.* [66] introduced gradient and direction vector flow, which is capable of addressing the issue of weak edge leakage in some cases. Kovacs *et al.* [67] proposed harris function based active contour external force for detecting complex boundaries with weak contrast and high curvatures.

### 0.2.3 A new external force: gradient vector convolution

To overcome the drawbacks of GVF model, we introduce a new external force named gradient vector convolution in this section. For any bounded  $g \in \mathbb{R}^2$ , the linear diffusion process  $u_t = \nabla^2 u$ ,  $u(x,0) = g(x)$  possesses the unique solution  $u(x,t) = (G_{\sqrt{2t}} \otimes g)(x)$ ,  $t > 0$ , where  $\otimes$  denotes convolution,  $G_{\sqrt{2t}}$  is the Gaussian kernel of standard deviation  $\sqrt{2t}$ . We argue that the solution of Eq. (0.16) can be approximated by convolving the  $\nabla f = [f_x, f_y]$  with a kernel. This convolution-based external force is referred to as gradient vector convolution (GVC). Followed by fast Fourier transform, this convolution operation can be implemented in real time and the snake model would benefit much from this property in computation time. Denote the convolution kernel by  $K_{con}$ , the GVC takes the following form:

$$\begin{cases} u(x,y) = K_{con} \otimes f_x \\ v(x,y) = K_{con} \otimes f_y \end{cases} \quad (0.17)$$

In practice, we take  $K_{con} = \frac{1}{(r_h)^n}$ , where  $r_h = \sqrt{x^2 + y^2 + h}$ ,  $h \in R^+$ ,  $n \in R^+$ .  $K_{con}$  always works well in terms of extending and smoothing gradient vector. Generally, the factor  $h$  plays a role that is analogous to scale space filtering. The greater the value of  $h$  is, the greater the smoothing effect on the results will be. This property suggests that GVC is robust to noise. In addition, large  $n$  makes the potential to degrade fast with distance and vice versa. Thereby it allows the GVC snake to preserve edges and to drive into C-shape concavities.

In order to well understand the behavior of  $h$  and  $n$ , we plot the proposed kernel  $K_{con}$  in 1D case with different  $h$  and  $n$  in Fig. 0.4. It can be seen from Fig. 0.4(a)

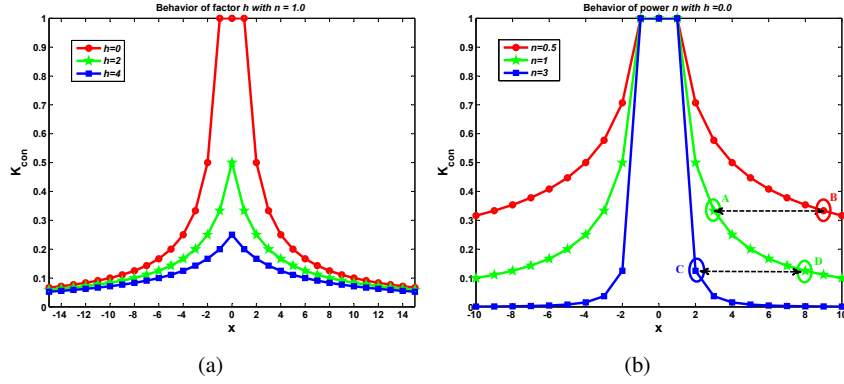
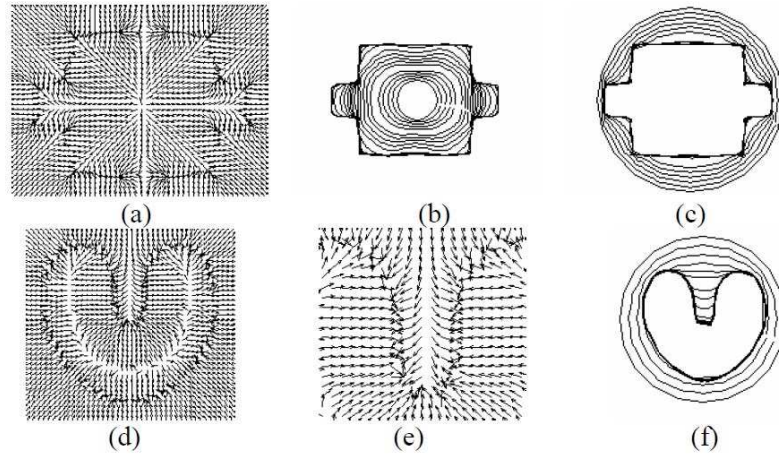


**Fig. 0.4** Analysis of the behavior of  $h$  and  $n$  in 1D case.

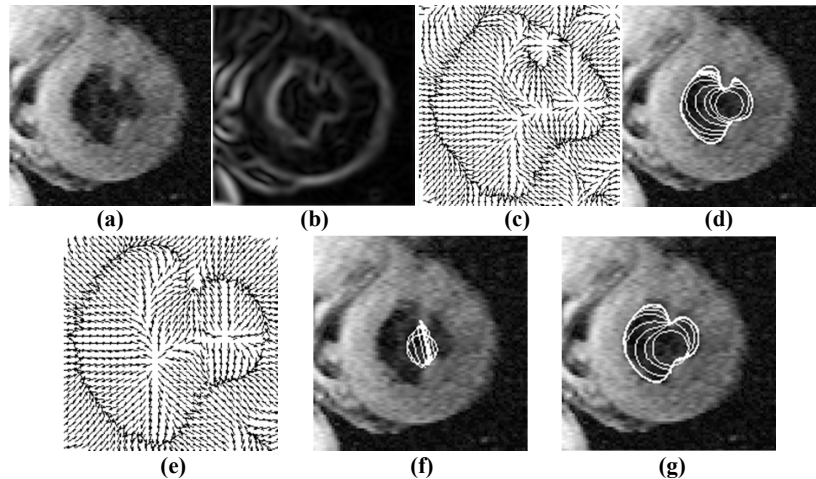
that, the larger the value of  $h$  is, the smaller the value of  $K_{con}$  at points nearby  $x = 0$  will be, but almost unchanged at points far from  $x = 0$ . Note that  $K_{con}$  is not defined at  $x = 0$  when  $h = 0$ , we set  $K_{con}(0) = K_{con}(1)$  for the sake of exhibition. Similar strategy is employed in Fig. 0.4(b). From Fig. 0.4(b), we can observe that the faster  $K_{con}$  degrades with distance as the value of  $n$  grows. For example, although point A is 3 while B which is far from  $x = 0$  is 9, due to varying  $n$ , the values of  $K_{con}$  at point A and B are almost identical. It seems as if the point B is as near as A to  $x = 0$  in terms of the value of  $K_{con}$ . Similar results can be observed for points C and D and it seems as if the point C is as far as D from  $x = 0$ . As a result, if one wants to separate two closely-neighbored objects or preserve edges, the large  $n$  can be used such that nearby points are less weighed as if they are far away. On the other hand, if the concavity is too deep, small  $n$  can be employed to weigh relatively more on faraway points as if they are nearby.

Fig. 0.5 shows two examples of the GVC snake. These experiments are implemented in MATLAB on an Intel Core2 2.66 GHz processor with 2GB RAM. The room and U-shape images are coined in [21] to demonstrate capture range enlarging and concavity convergence. The size of both images is  $64 \times 64$ . The parameters for GVC are  $h = 0$ ,  $n = 2.0$ , the kernel size is the same as that of the image. The GVC is able to obtain similar results as the GVF (see [21]). It is worth noting that the execution time of GVC for both images is 0.027s while that of GVF is 2.36s with 50 iterations.

As a second example, a comparative study of GVC and GVF is conducted on the heart image used in [21], shown in Fig.0.6 (a). The heart image is first blurred with a Gaussian kernel with standard deviation 3.0, and the edge map is shown in Fig.0.6 (b). The GVC is calculated with  $n = 2.0$ ,  $h = 2.0$ , and execution time is 0.531s, as shown in Fig.0.6 (c). A circle is used as initial contour, the snake contour can correctly locate the left ventricle and the result is in Fig.0.6 (d). The GVF is also calculated, for all GVF in this experiment,  $\mu = 0.15$  and time step is 0.5. Fig.0.6 (e) presents the GVF after 200 iterations, and execution time is 6.407s.



**Fig. 0.5** The performance of GVC snake on U-shape and room images. (a) is the GVC field of room image; (b) and (c) are the convergence of the GVC snakes with the initial contours inside and outside the room, respectively; (d) is the GVC field of U-shape image; (e) is the close-up of GVC field within the concavity; (f) is the convergence of the GVC snake on the U-shape image.



**Fig. 0.6** Comparison of GVC and GVF on the heart image.

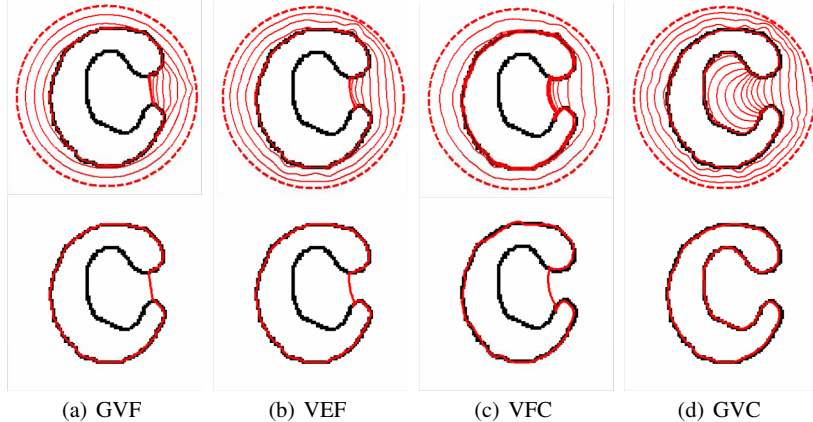


**Fig. 0.7** Comparisons of C-shape image convergence on GVF, VEF, VFC and GVC snakes. Note that the dashed red lines represent the initial curves, and the solid red lines denote the final active contours.

The same circle as in Fig.0.6 (d) is used as initialization, but due to the critical points in GVF [68], the snake contour collapses to a tangled curve, see Fig.0.6 (f), therefore, a larger circle including the critical points is employed as initialization and the segmentation result is fairly satisfactory, see Fig.0.6 (g). This result implies that the critical point issue of GVC snake is less serious than that of the GVF snake. In addition, comparing Fig.0.6 (d) and (g), although the initial contour in Fig.0.6 (g) is larger, but the segmentation result of the GVC snake is much better than that of the GVF snake. We also observe this phenomenon in the room image that GVC snake can detect the corner more accurately than that of the GVF snake. What's more, let us keep in mind: *the computation time of the GVC is much shorter than that of the GVF*.

Furthermore, we use the C-shape image of  $256 \times 256$  pixels to verify the performance of the GVC snake on concavity convergence. We apply the GVF [21], VEF [69] , VFC [22] and GVC snakes to a C-shape image, as shown in Fig. 0.7. The difference between C-shape concavity and U-shape concavity is that the C-shape is semi-close, while the U-shape is open. The results show that the GVC snake evolves into the concave region progressively, steadily and correctly. In contrast, others fail. The success of GVC snake is ascribed to the larger weight on faraway points with a small  $n$ . The parameters of GVC snake are:  $\alpha = 0.5$ ,  $\beta = 0.5$ , time step  $\tau = 1$  ,  $h = 1$  and  $n = 2.6$ .

### 0.3 Automatic localization of the LV

In a short-axis view of cardiac MR images, the myocardium is a dark area between two concentric circles enclosing a bright area corresponding to the blood in LV. On its left side is a bright region corresponding to the blood in RV. On its right side is a very dark area corresponding to the lungs. Under breath-hold condition, LV moves more obviously than its surrounding structures that are almost static during the cardiac cycle. This trait encourages intensity difference algorithm upon two consecutive frames in temporal image sequences to remove stationary background structures, and then localizes the moving region of the left ventricle.

To more robustly localize the LV, we adopt the fourth-order partial differential equations (PDEs) for noise removal [70]. The Euler equation of fourth-order PDEs is expressed as

$$\frac{\partial I}{\partial t} = -\nabla^2 [c(|\nabla^2 I|)\nabla^2 I], \quad (0.18)$$

where  $\nabla^2$  denotes Laplacian operator, and  $c(\cdot)$  is a nonnegative and decreasing function. In this study,  $c(\cdot)$  is given by

$$c(|\nabla^2 I|) = \left(1 + \left(\frac{\nabla^2 I}{h}\right)^2\right)^{-1}. \quad (0.19)$$

This anisotropic diffusion can selectively smooth the image to preserve the object edge and to remove the noise within homogeneous regions. Applying Eq. (0.18) to cardiac MR images, the myocardium region would be highlighted.

Suppose a cardiac MR images sequence  $I_t(x,y)$ , where  $(x,y)$  denotes the spatial coordinates of an image and  $t \in T$  is the time instant. The nearly non-moving background pixels in two consecutive frames are excluded by the difference or subtraction operation defined as

$$D(x,y) = [I_{t+1}(x,y) - I_t(x,y)] > Th. \quad (0.20)$$

Here  $D(x,y)$  is the intensity difference image,  $Th$  is a threshold value which we consider as non-moving background.  $Th$  is estimated by the OTSU method [71]. Observing the Fig. 0.8, the intensity values near the myocardial boundaries are different from those in other regions because of larger movement of the LV. The dense highlighted circle-like region implies that the endocardium moves faster than the epicardium. Applying Hough transform to the difference image, we can obtain the LV centroid and the region of interest represented by a yellow solid circle.

### 0.4 Segmentation of the endocardium

Though MRI provides quite good contrast between the myocardium and the blood pool, the difficulties in segmenting the endocardium originate primarily from arti-

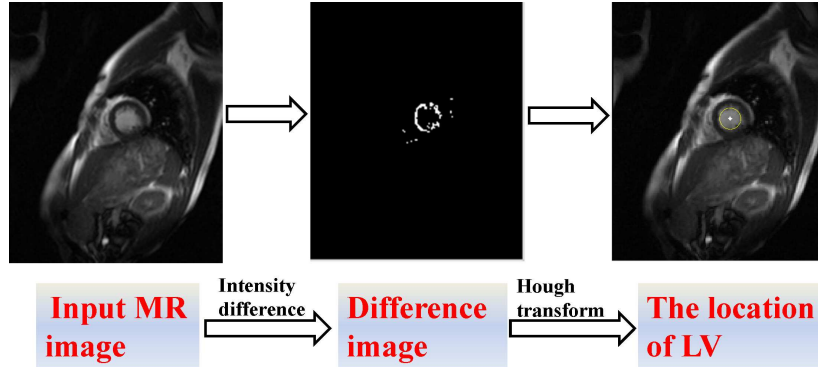


**Fig. 0.8** Automatic localization of the LV.

facts and papillary muscles. In the classical internal energy of snake model (see Eq. (0.1)), the first and second derivatives control the continuity and smoothness of the curve, respectively. However, continuity and smoothness are only local geometrical properties. For example, if there exist weak boundaries, the snake contour is not able to bridge such gaps in which there is no prior information accounting for the holistic shape of an object. In addition, if there are local minima caused by imperfection of the external force, the snake contour would be strapped. A solution to these issues is to incorporate the shape prior into snake energies. Observed that the endocardium of the LV is roughly a circle, a circle-shape constraint [72] is adopted for the endocardium segmentation. It is formulated as

$$E_{endo} = \frac{\lambda}{2} \int_0^1 (R(s) - \bar{R})^2 ds, \quad (0.21)$$

where

$$\left\{ \begin{array}{l} R(s) = \sqrt{(x(s) - x_c)^2 + (y(s) - y_c)^2} \\ x_c = \int_0^1 x(s) ds \\ y_c = \int_0^1 y(s) ds \\ \bar{R} = \int_0^1 R(s) ds . \end{array} \right.$$

$(x_c, y_c)$  is the centroid of the snake contour. The energy Eq. (0.21) measures the deviation of the snake contour from a circle with radius  $\bar{R}$  and center  $(x_c, y_c)$ . Both  $\bar{R}$  and  $(x_c, y_c)$  are dynamic with the evolution of the snake contour. If the snake contour is attracted by artifacts or papillary muscle, this constraint would penalize the snake contour to be a circle, thus, the global shape of the LV would be maintained.

Suppose that there are  $n$  discrete points on the snake contour, the center  $(x_c, y_c)$  can be estimated by the following equations

$$\left\{ \begin{array}{l} x_c = \frac{1}{n} \sum_{i=1}^n x_i \\ y_c = \frac{1}{n} \sum_{i=1}^n y_i \\ R(i) = \sqrt{(x_i - x_c)^2 + (y_i - y_c)^2} \\ \bar{R} = \frac{1}{n} \sum_{i=1}^n R_i , \end{array} \right.$$

where  $i = 1, 2, \dots, n$ . Since

$$\left\{ \begin{array}{l} (R(s) - \bar{R})^2 = (R(s) - \bar{R})^2 (\cos^2(2\pi s) + \sin^2(2\pi s)) \\ = (R(s) \cos(2\pi s) - \bar{R} \cos(2\pi s))^2 + (R(s) \sin(2\pi s) - \bar{R} \sin(2\pi s))^2 \\ R(s) \cos(2\pi s) = x(s) - x_c \\ R(s) \sin(2\pi s) = y(s) - y_c, \end{array} \right.$$

by the calculus of variation, the discrete Euler equation of Eq. (0.21) is given by

$$\left\{ \begin{array}{l} \lambda(x_i - x_c - \bar{R} \cos(2\pi i/n)) = 0 \\ \lambda(y_i - y_c - \bar{R} \sin(2\pi i/n)) = 0 . \end{array} \right. \quad (0.22)$$

The solution of Eq. (0.22) obtained by treating  $x$  and  $y$  as the functions of time  $t$  is expressed as

$$\left\{ \begin{array}{l} \frac{x_i^{t+1} - x_i^t}{\Delta t} + \lambda x_i^{t+1} - \lambda(x_c^t + \bar{R}^t \cos(2\pi i/n)) = 0 \\ \frac{y_i^{t+1} - y_i^t}{\Delta t} + \lambda y_i^{t+1} - \lambda(y_c^t + \bar{R}^t \sin(2\pi i/n)) = 0 . \end{array} \right. \quad (0.23)$$

Eq. (0.2) will collaborate with Eq. (0.23) to extract the endocardium, and the force vector  $-\nabla g(C(s))$  in Eq. (0.2) will be replaced by  $[u(x, y), v(x, y)]$  in Eq. (0.17).

## 0.5 Segmentation of the epicardium

The contrast between the myocardium and surrounding tissues (e.g. fat, lung and liver) is poor, and thus it would be more difficult to segment the epicardium [18]. In practice, the segmented endocardium would be beneficial significantly to segment the epicardium. We exploit the relationship between the endocardium and the

epicardium in shape and position for the epicardium segmentation in the following aspects: (1) using the endocardium result as initialization to automatically segment the epicardium; (2) the endocardium is always encircled by or nearby the epicardium so that one can build new external force according to this position relationship; (3) the endocardium usually resembles the epicardium in shape, thus, the endocardium may serve as a priori shape to guide the segmentation of the epicardium. With these strategies, the epicardium is automatically extracted after the endocardium is segmented.

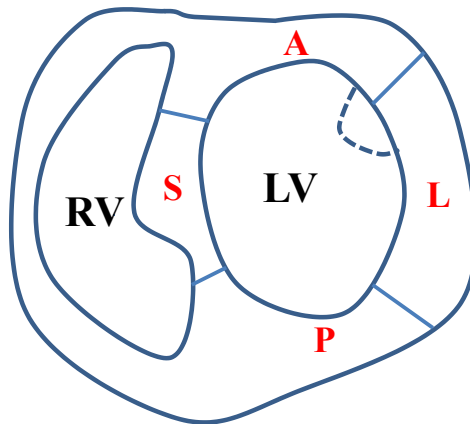


**Fig. 0.9** Illustration of cardiac anatomy.

### 0.5.1 The epicardium segmentation strategy: 1

**A: Adaptation to epicardium** The energy Eq. (0.21) regularizes the snake to a canonical circle, but for the epicardium, the uniformly weighted circle shape constraint would cause poor performance because the left ventricle is not exactly a circle but more like an oval and there are gaps on the epicardium boundary as well. As illustrated in Fig. 0.9, the LV can be generally divided into four partitions: septum, anterior, lateral and posterior, denoted as “S”, “A”, “L”, and “P”, respectively. The boundary at septum interfacing the RV is salient; the anterior and posterior parts are in junction with the RV and the boundaries there are fraudulent; the lateral part interfaces the lung and the boundaries there are usually not as salient as at septum, possibly very weak. When the circle shape energy is applied uniformly, it would be too strong for some parts but too weak for others, so, we employ different weights for different partitions as  $\lambda_S$ ,  $\lambda_A$ ,  $\lambda_L$ ,  $\lambda_P$ . In practice, more weights can be adopted

according to the image quality, for instance, the posterior also partially neighbors other organs, therefore, one more weight can be associated to it.

**B: External force for epicardium segmentation** Because the endocardium is a local minimum of the GVF field, the snake contour would become stationary there and it is impossible to extract the epicardium successively after the endocardium is located. But as far as we know, among the existent studies based on GVF snake, there is one exception in; however, it is not clear how their method sequentially “*search for the first local minimum that is expected to correspond to the epicardium surface*”. In this study, we develop a novel strategy to erase the endocardium, and then generate the external force for epicardium locating.

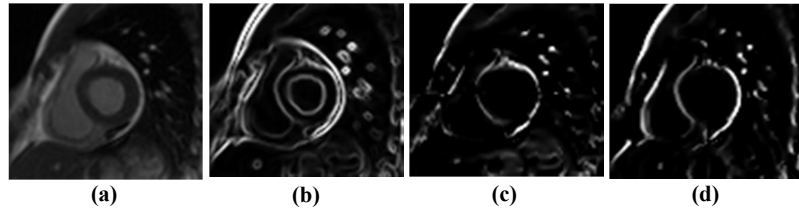


**Fig. 0.10** Edge maps for epicardium locating.

We take the center of the endocardium as reference and generate two edge maps by selectively choosing the gradient in direction of  $x$  and  $y$  according to the characteristics of the image. Taking the image in Fig. 0.10 (a) as an example, on the left of the center, the septum interfaces the blood pools of RV and LV, the gradient in direction of  $x$  is taken as  $f_l^x = |\min(I_x, 0)|$  such that the edge between septum and the LV blood pool is neglected; but for the right part, the gradient is  $f_r^x = |\max(I_x, 0)|$  while the lateral is surrounded by fat (if no fat, choosing  $f_r^x = |\min(I_x, 0)|$ ), thus, the edge between lateral and the LV blood pool and the one between the fat and the lung are neglected. Likewise, the gradient in direction of  $y$  up and down the center are  $f_u^y = |\min(I_y, 0)|$  and  $f_d^y = |\min(I_y, 0)|$ . Then  $f_x$  and  $f_y$  are utilized as edge maps to calculate GVC external force.

Fig. 0.10 shows the edge maps derived from this strategy, (b) is the usual edge map, and (c) and (d) are  $f_x$  and  $f_y$ , respectively. Generally speaking, this method is robust to noise because the min-max operation can weaken the side effects of noise; meanwhile, it depends on the characteristics of the image which should be known in advance.

We also applied the proposed strategies to a set of short-axis in vivo data. In our dataset, there are seven image slices spanning the whole left ventricle, and there are 20 images acquired throughout one cardiac cycle each slice. The scanning protocol will be introduced in Sec. 0.6.1. The parameters of the snake model for endocardium are  $\alpha = 1$ ,  $\beta = 1$  and  $\lambda = 0.5$ . The parameters for epicardium are  $\alpha = 1$ ,  $\beta = 1$ ,  $\lambda_S = 0$ ,  $\lambda_A = 1$ ,  $\lambda_L = 0.5$ ,  $\lambda_P = 1$ ,  $h = 8$ , and  $n = 2.6$ .

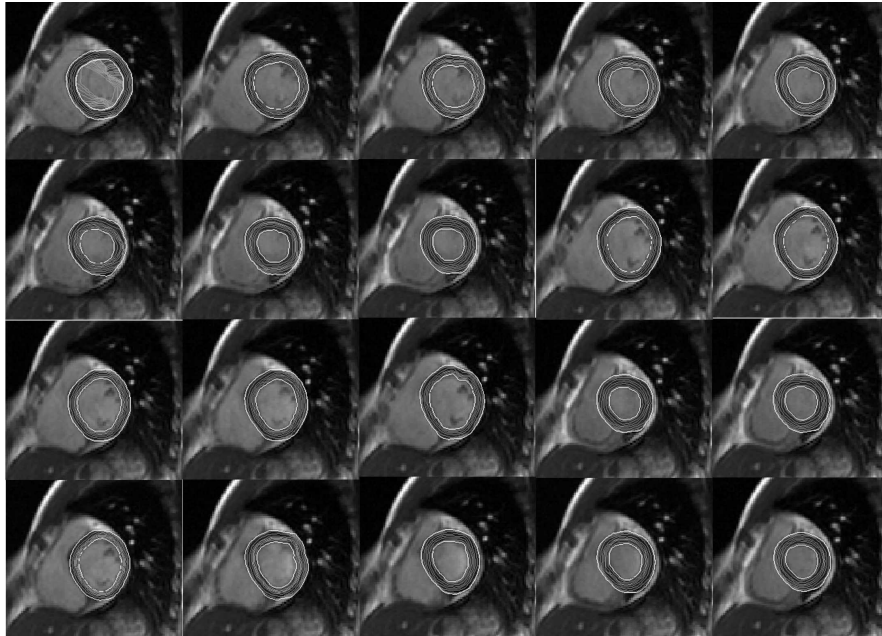


**Fig. 0.11** Segmentation of the left ventricle in our dataset.

### 0.5.2 *The epicardium segmentation strategy: 2*

**A: External force for epicardium segmentation** Since the endocardium is a local minimum, this prevents the GVC active contour moving into the boundary of epicardium. In order to extract automatically the epicardium by taking the endocardium as initialization, the local minimum stemming from the endocardium edge should be filtered out. To this end, we directly set the original edge map around and within the endocardium to zero. This modified edge map is used to generate a new GVC force field, which leads to the fact that the endocardium is no longer a local minimum of the new GVC force. This new GVC force, thus, can push the endocardium forward to the epicardium directly. In addition, since the endocardium and epicardium are adjacent, the capture range of the new GVC force needs not to be very large, so it takes even shorter time to calculate.

Fig. 0.12 illustrates the effectiveness of the modified edge map for the epicardium segmentation. From left to right, the upper row in Fig. 0.12 shows the original edge map, the GVC field and the segmentation result, respectively. Since the myocardium is thin and the initial contour should avoid critical points in the force field [68], it is feasible to segment the epicardium using the original force field. Moreover, the original force field flows into the myocardium at the weak epicardium boundaries ( see the white ellipse on the upper row in Fig. 0.12). In contrast, when the edge

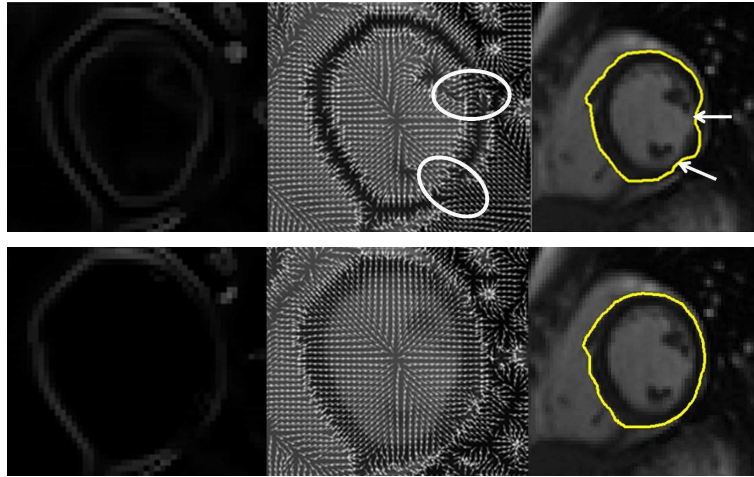


**Fig. 0.12** Comparisons of external force for epicardium segmentation. The upper row: the original edge map. The lower row: the modified edge map.

map is modified using the proposed strategy, as shown in lower row in Fig. 0.12, the associated force field can characterize the epicardium very well.

**B: Internal force for the epicardium segmentation** Generally speaking, there would be spurious edges on the myocardium, and the contrast between myocardium and surrounding structures is low. Even though the endocardium edge is removed, the new external force would not be good enough to prevent the snake contour from leaking out from weak boundaries. In order to get a more accurate segmentation result of the epicardium, we employ the endocardium result as *a priori* shape and construct a new shape-similarity based constraint given by

$$E_{epi} = \frac{\rho}{2} \int_0^1 ((R(s) - \bar{R}) - (r(s) - \bar{r}))^2 ds. \quad (0.24)$$

The variables in Eq. (0.24) have similar meanings as in Eq. (0.21), but  $R$  and  $\bar{R}$  are for epicardium while  $r$  and  $\bar{r}$  are for segmented endocardium. The snake contour for epicardium is supposed to be identically centered with the endocardium. It is clear in Sect. 0.4 that  $r(s_i) - \bar{r}$  measures the deviation of the endocardium contour from a circle with radius  $\bar{r}$  at snaxel  $s_i$ , thus  $R(s_i) - \bar{R}$  measures the deviation of the snake contour for epicardium from a circle with radius  $\bar{R}$  at snaxel  $s_i$ . Minimizing the energy  $E_{epi}$  will make two deviations small, finally the snake contour for epicardium will resemble the endocardium in shape although their scales, i.e.,  $\bar{R}$  and  $\bar{r}$  are different.

Similar to Eq. (0.21), by the calculus of variation, we obtain the Euler equation for Eq. (0.24) as follows:

$$\begin{cases} \rho(x_s - x^{endo}(s) - (\bar{R} - \bar{r}) \cos(2\pi s)) = 0 \\ \rho(y_s - y^{endo}(s) - (\bar{R} - \bar{r}) \sin(2\pi s)) = 0 . \end{cases} \quad (0.25)$$

It is discretized as

$$\begin{cases} \rho(x_i - x_i^{endo} - (\bar{R} - \bar{r}) \cos(2\pi i/n)) = 0 \\ \rho(y_i - y_i^{endo} - (\bar{R} - \bar{r}) \sin(2\pi i/n)) = 0 . \end{cases} \quad (0.26)$$

This equation can be solved in the same way as Eq. (0.23) by taking  $x$  and  $y$  as the function of time  $t$ . Similarly, Eq. (0.2) will collaborate with Eq. (0.26) to extract the epicardium, and the force vector  $-\nabla g(C(s))$  in Eq. (0.2) will be replaced by  $[u(x, y), v(x, y)]$  in Eq. (0.17) using the modified edge map in Sect. 0.5.1.

## 0.6 Experiment results

To evaluate the performance of the proposed algorithm, we compare our method with three shape-based snake methods including the Radial GVF Snake (referred to as RGVF) [13], level-set method (referred to as LSM) [11] and max-flow method (referred to as MFM) [2]. The parameters of our model are  $\alpha = 0.5$ ,  $\beta = 0.5$ ,  $\lambda = 0.4$ ,  $\rho = 1.2$ ,  $h = 8$  and  $n = 2.6$ . The parameters of RGVF model are  $\alpha = 1$ ,  $\beta = 1$ ,  $\gamma = 1$  and  $\eta = 0.5$ . The parameters of LSM are  $\alpha = 1000$ ,  $\beta = 10$ ,  $\lambda = 0.1$  and  $c = 10$ . The parameters of MFM are  $\gamma = 1$ ,  $\lambda = 0.0011$ .

### 0.6.1 Experiment data

In our experiments, we test the above-mentioned methods on two datasets: *MICCAI 2009* and our own dataset. Cardiac cine MRI data of *MICCAI 2009* is provided by the *MICCAI 2009* Cardiac MR LV Segmentation Challenge organizers. The scanning protocol and evaluation criterion of this dataset are fully described in [57]. Images of our own dataset (126 images) were acquired using a 1.5T Siemens MRI scanner from a healthy volunteer. Typical parameters were TR: 29.16 ms; TE: 1.08 ms; flip angle: 50°; image dimension: 192 × 156; typical spatial resolution: 1.82 × 1.82 mm<sup>2</sup> in-plane; and slice thickness: 8 mm. There are 7 slices covering the entire LV from the apex to the base, and 21 cardiac phases in each slice.

### 0.6.2 Evaluation criteria

In this paper, we evaluate the RGVF, LSM, MFM and our methods qualitatively and quantitatively. For qualitative assessments, we present representative segmentation

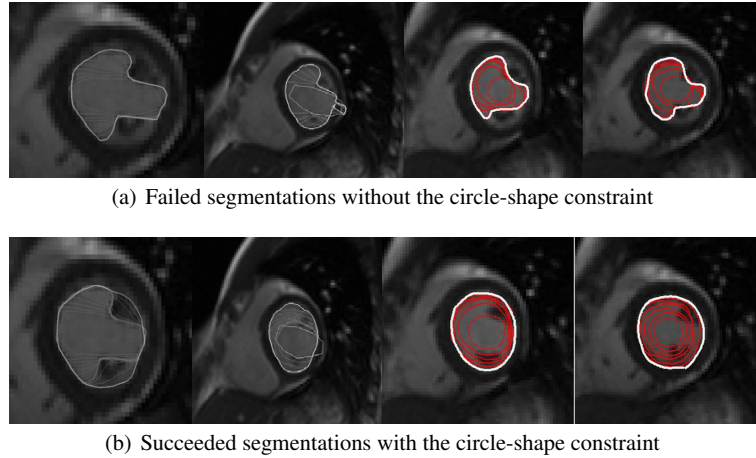


**Fig. 0.13** Effectiveness of the circle-shape energy for endocardium segmentation.

results from each dataset. For quantitative evaluation, we use the mean absolute distance (MAD) [73] as well as the Dice metric (DM) [2]. Suppose there are  $n$  points on the snake contour denoted by  $S = \{s_1, s_2, \dots, s_n\}$ ,  $k$  points on the ground truth expressed as  $M = \{m_1, m_2, \dots, m_k\}$ , the MAD is defined as

$$MAD(S, M) = \frac{1}{2} \left( \frac{1}{n} \sum_{i=1}^n d(s_i, M) + \frac{1}{k} \sum_{j=1}^k d(m_j, S) \right), \quad (0.27)$$

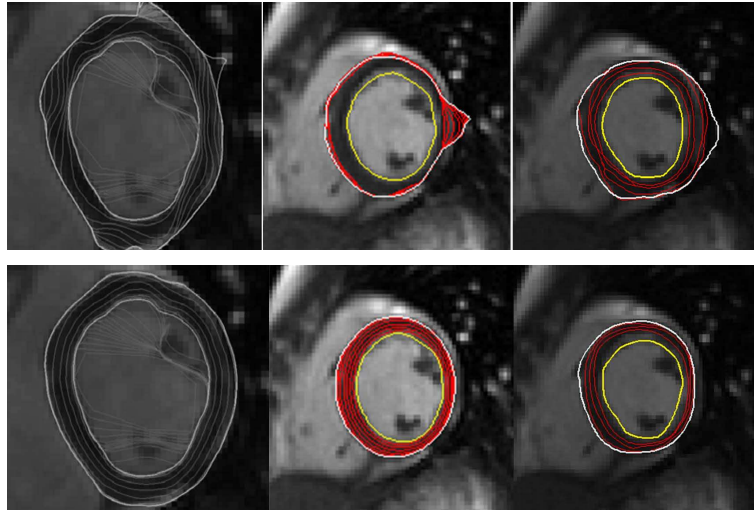
where  $d(s_i, M) = \min_j \|s_i - s_j\|$  is the distance from point  $s_i$  to the closest point on contour  $M$ . The Dice metric (DM) [2] is a measure of contour overlap utilizing the contour areas automatically segmented  $A_a$ , manually segmented  $A_m$ , and their intersection  $A_{am}$ . It is given by

$$DM = 2A_{am} (A_a + A_m)^{-1}. \quad (0.28)$$

DM is always between 0 and 1, with higher DM indicating better match between automatic and manual segmentations.

### 0.6.3 The effectiveness of the shape based constraints

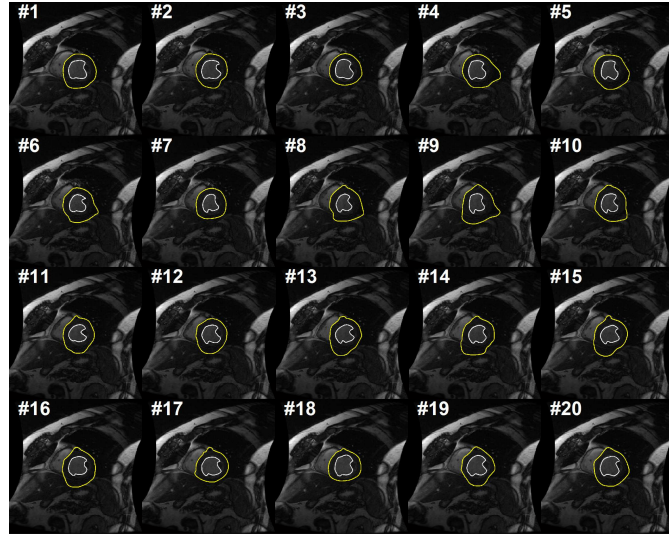
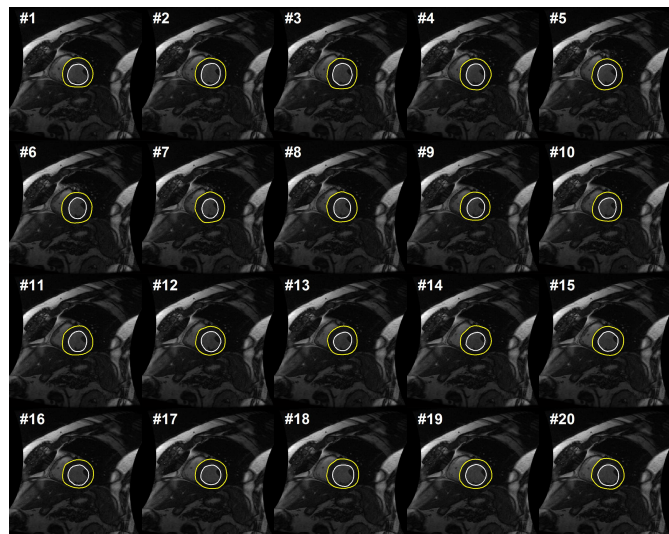
In this section, we demonstrate the effectiveness of the proposed circle-shape constraint and the shape-similarity constraint for segmenting the LV. Fig. 0.13 illustrates segmentation results of the endocardium using the circle-shape energy to conquer the papillary muscle and artifacts. The images are taken from mid-ventricle slice, where the papillary muscles are obstacles for the GVC snake model. When the initial contour excludes the papillary muscles, the snake contour halts at the papillary



**Fig. 0.14** Effectiveness of the shape-similarity based constraint for epicardium segmentation. The upper row: without the shape-similarity based constraint. The lower row: with the shape-similarity based constraint.

muscles and artifacts (see Fig. 0.13(a)) unless the initial contour is close enough to the endocardium. In contrast, when the global shape constraint is incorporated into the GVC snake model, the snake contour conquers the papillary muscles successfully and sticks to the endocardium (see Fig. 0.13(b)). In addition, we demonstrate the effectiveness of the shape similarity energy for epicardium extraction, as shown in Fig. 0.14. Although the enhanced external force characterizes the epicardium very well, the result in the upper row of Fig. 0.14 leaked out due to the nearby artifacts in the lung region. In contrast, when the shape similarity energy is incorporated, the snake contour works well to delineate the epicardium (see the lower row of Fig. 0.14).

Figure. 0.15 depicts the segmentation results of LV with and without shape prior information on *MICCAI 2009* dataset. Without shape based constraint, the external force field pulls the snake to a false contour shown in Fig. 0.15(a). These results are hardly to be accepted. Fig. 0.15(b) shows that the shape based energy functionals presented in Eq. (0.21) and Eq. (0.24) are efficient to push the snake contours to the desire solution. Figure. 0.16 illustrates the MAD errors corresponding to Fig. 0.15 of one subject on *MICCAI 2009* dataset with and without constraints. Overall, the shape information of LV is integrated to the GVC snake model to effectively alleviate the effect of papillary muscle and noise, and to prevent the snake contour from leaking out from weak boundaries.

(a) The segmentation results of the LV **without** shape based constraints(b) The segmentation results of the LV **with** shape based constraints**Fig. 0.15** Effectiveness of the shape based constraints for the LV segmentation.

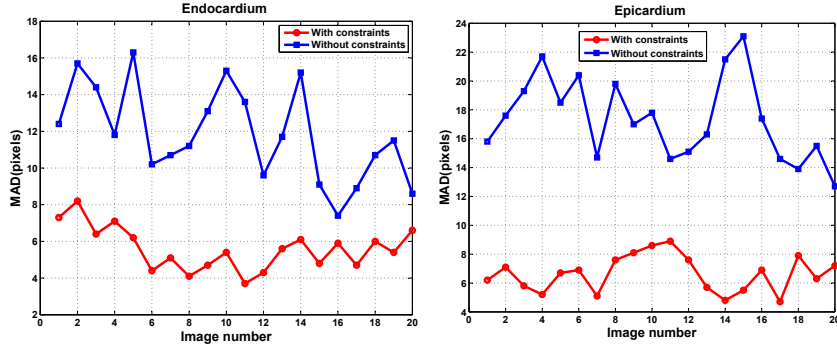


**Fig. 0.16** The MAD errors corresponding to Fig. 0.15 of one subject on *MICCAI 2009* dataset with and without shape based constraints.

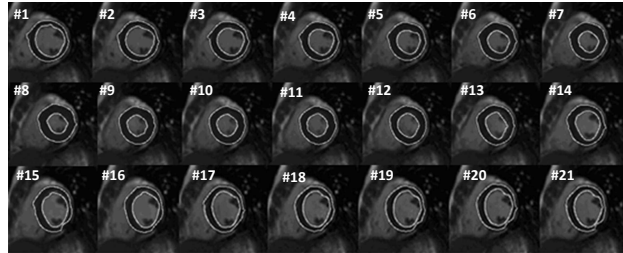
#### 0.6.4 Comparison with the state-of-the-arts

From the qualitative comparisons depicted in Fig. 0.17, we can see that the segmentation results of both LSM and RGVF methods are noticeably worse than those of both MFM and our methods, at some frames (such as around the frames 9, 19, 20 and 21). It can be explained that the LSM method is based on the assumption that the *overlap* is approximately constant, thus a high variation of the *overlap* in the given sequence will affect segmentation accuracy. Since the myocardium is thin during ventricular diastole, the RGVF contour is evaluated along 1D radial direction rather than 2D image plane, as a result, the segmented contour is sensitive to the neighbor organs such as the liver. In contrast, The MFM and our methods obtain good results.

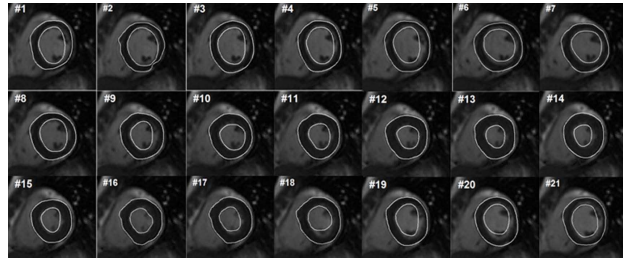
**Table 0.1** Quantitative performance evaluations on our own dataset (126 images) for RGVF [13], LSM [11], MFM [2] and our methods. The first two rows denote the statistics of the DM given by mean  $\pm$  standard deviation. The second two rows are average MAD (in pixels).

	RGVF	LSM	MFM	Ours
Cavity DM	$0.83 \pm 0.046$	$0.80 \pm 0.021$	$0.86 \pm 0.011$	$0.84 \pm 0.019$
Myocardium DM	$0.76 \pm 0.126$	$0.84 \pm 0.032$	$0.83 \pm 0.027$	$0.85 \pm 0.053$
Endocardium MAD	1.3952	3.7667	1.1238	1.1190
Epicardium MAD	3.5333	2.8048	1.2238	1.1333

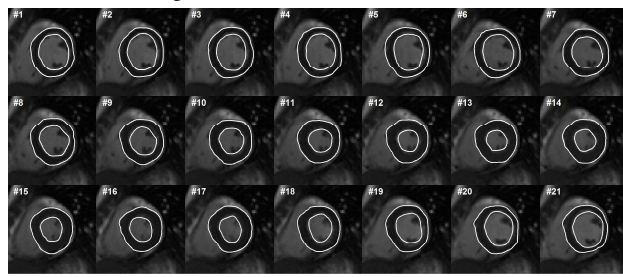
Table. 0.1 and Fig. 0.18 show quantitative evaluations on our own dataset (126 images) for RGVF, MFM, LSM and our methods. The first two rows in Table. 0.1 report the DM statistics, where DM is given by mean  $\pm$  standard deviation. For the cavity detection, MFM and our methods lead to a region accuracy slightly better than both LSM and RGVF methods. The second two rows in Table. 0.1 show average



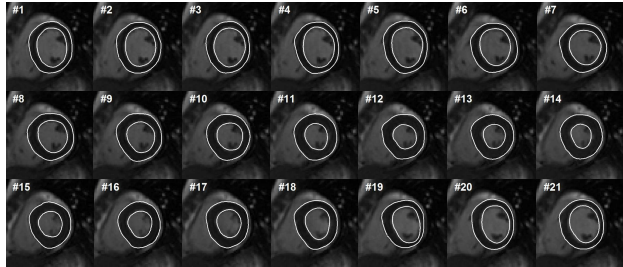
(a) The segmentation results of the LV with RGVF method [13]



(b) The segmentation results with LSM method [11]



(c) The segmentation results with MFM method [2]



(d) The segmentation results with our method

**Fig. 0.17** Qualitative results of one subject on our own dataset.

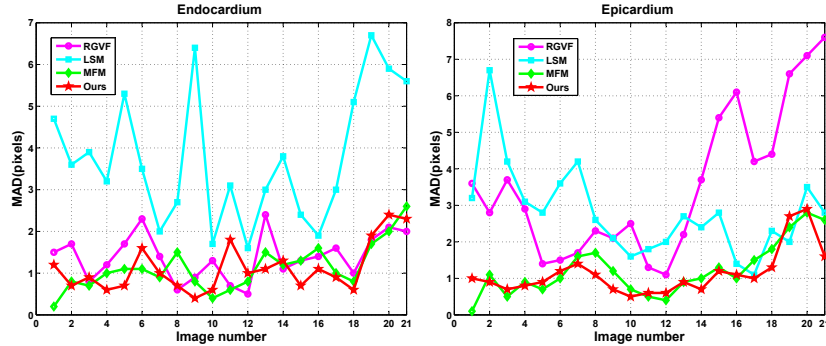


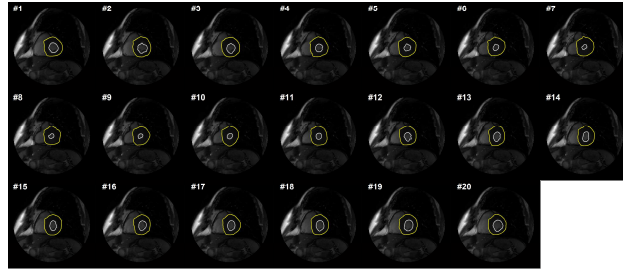
**Fig. 0.18** Quantitative results corresponding to Fig. 0.17 of one subject on our own dataset.

MAD (in pixels) of these models. We see that our method outperforms the other approaches.

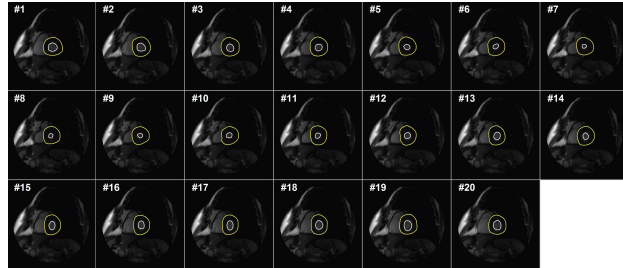
We also run our algorithm on the *MICCAI 2009* dataset. Look from visuality, these methods obtain similar results, as shown in Fig. 0.19. However, our method is able to achieve much more accurate and consistent segmentation results, as shown in Fig. 0.20. The average MAD of RGVF, LSM, MFM and our methods for the endocardium segmentation are 9.06 pixels, 7.21 pixels, 4.79 pixels and 5.06 pixels, respectively, and those of the epicardium are 7.85 pixels, 5.70 pixels, 5.23 pixels and 5.18 pixels, respectively. Overall, the proposed method could conquer image noise, artifacts, weak boundaries and papillary muscles perfectly on both endocardial and epicardial boundaries extraction. Nevertheless, our method remains great MAD errors during segmenting the endocardium, especially at the frames 7, 13 and 17. Around at these frames, the blood pool has almost the same intensity profile (*e.g.* the papillary muscles within the cavity and the myocardium). More representative images on *MICCAI 2009* dataset are shown in Fig. 0.21.

### 0.6.5 Discussion

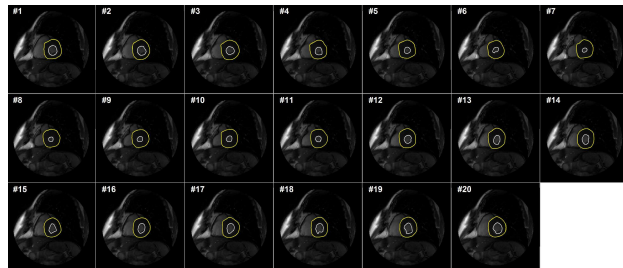
Although the results obtained by our method are desirable, one significant assumption is that the shape of the LV is pre-defined circularly. This assumption limits a more extensive exploration of our method for the LV segmentation. Moreover, A major difficulty in segmentation of MR images is the intensity inhomogeneity due to the radio-frequency coils or acquisition sequences. There exists the inefficiency in handling images with *severe* intensity inhomogeneity. Fig. 0.22 shows failed segmentation cases of our method, in which the myocardium and its neighbor organs such as the liver are connected, resulting in the same intensity profile. Segmenting such region of interest is extremely difficult because the contour is almost indistinguishable in this situation, even for human eyes. Different from the MFM method



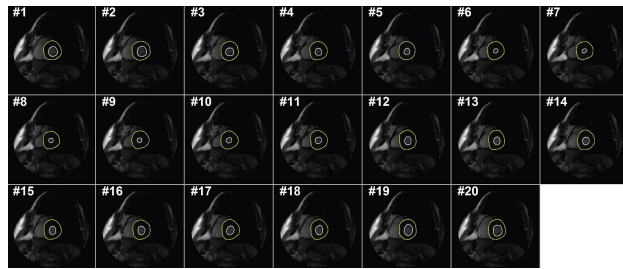
(a) The segmentation results of RGVF method [13]



(b) The segmentation results of LSM method [11]



(c) The segmentation results of MFM method [2]



(d) The segmentation results of our approach

**Fig. 0.19** Qualitative results of one subject on *MICCAI 2009* dataset.

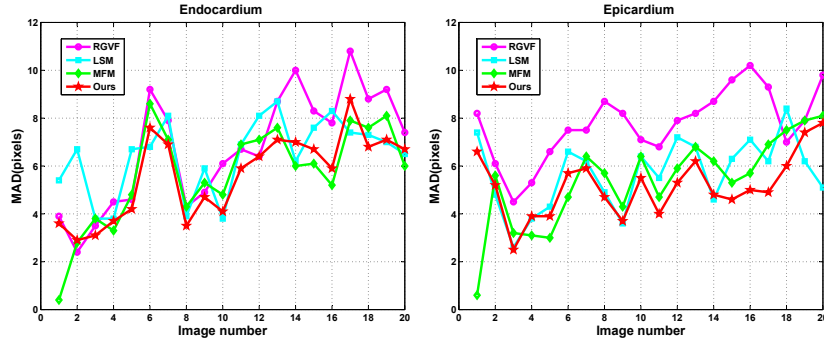


**Fig. 0.20** Quantitative results corresponding to Fig. 0.19 of one subject on *MICCAI 2009* dataset.

[2], the proposed approach requires a large number of iterative updates of the segmentation, thus, is computationally onerous. Running on a Intel Core2 2.66 GHz processor with 2GB RAM, on average, our implementation needs 4.76s to process a frame of  $256 \times 256$  pixels. These issues motivate us to develop a more efficient LV segmentation algorithm in future.

## 0.7 Conclusion

We have presented an automatic algorithm for left ventricle segmentation in cardiac cine MRI based on the gradient vector convolution (GVC) snake model. The GVC model possesses similar properties of the GVF model and it can be implemented in real time due to its convolutional nature. Based on GVC snake model, Hough transform is first applied to intensity difference image computed between two consecutive frames in temporal image sequences to locate LV centroid and the region of interest (ROI). A circle-shape based energy is integrated into the snake model for extracting the endocardium to conquer papillary muscle and artifacts. After endocardium extraction, both the GVC external force modified skillfully and shape-similarity based constraint reactivate the snake contour forward to epicardial contour successively. Comparative results on both our dataset and the *MICCAI 2009* dataset demonstrated a good performance of the proposed segmentation approach against the state-of-the-art methods.

## Acknowledgments

The authors would like to thank both the editor and the reviewers for the invaluable comments and suggestions that help a great deal in improving the manuscript. This

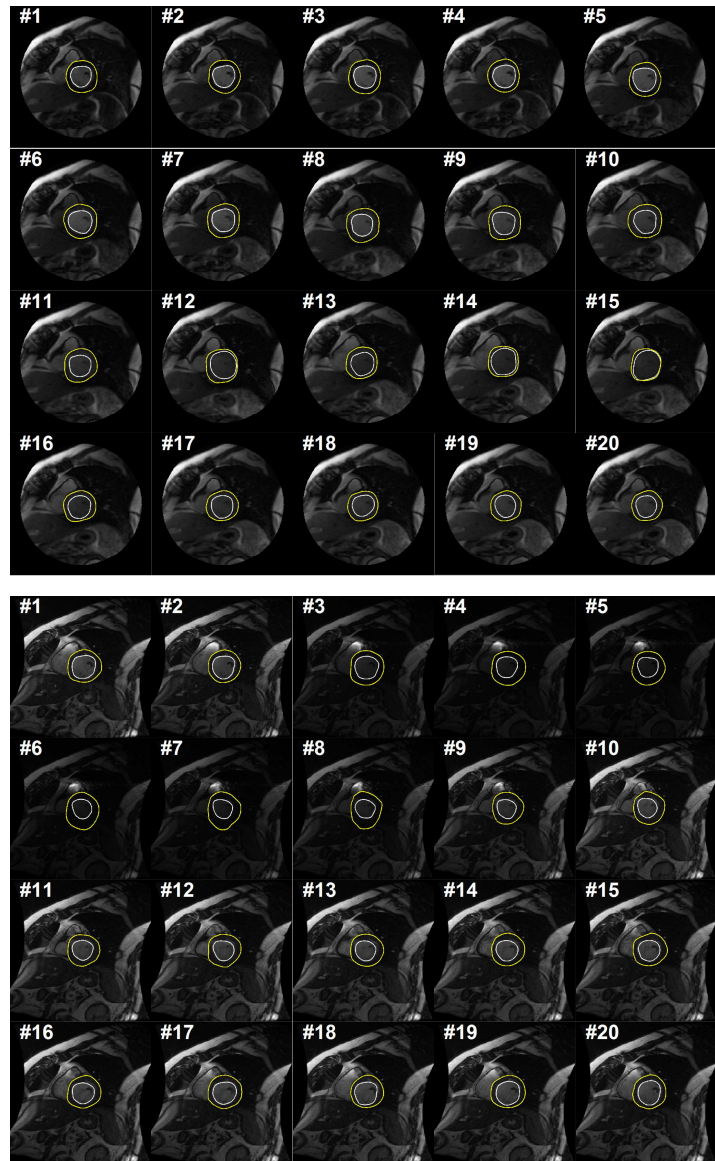


**Fig. 0.21** More experiment results of our method on *MICCAI 2009* dataset.

work was supported in part by the Natural Science Foundation of China(NSFC) under Grants No.90920009 & No. 60602050, and the Key Program from the Tianjin Commission of Technology of China under Grant No. 11JCZDJC15600.

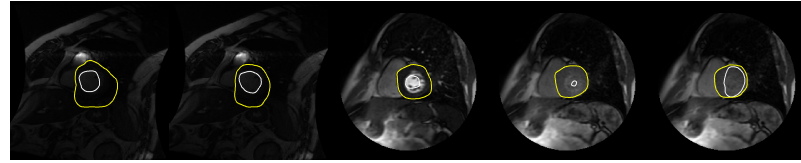


**Fig. 0.22** Failed segmentation cases of our method.

## References

1. Frangi, A., Niessen, W., Viergever, M.: Three-dimensional modeling for functional analysis of cardiac images, a review. *Medical Imaging, IEEE Transactions on* **20**(1) (2001) 2–5
2. Ayed, I., Chen, H., Punithakumar, K., Ross, I., Li, S.: Max-flow segmentation of the left ventricle by recovering subject-specific distributions via a bound of the bhattacharyya measure. *Medical Image Analysis* **16** (2012) 87–100
3. Punithakumar, K., Ben Ayed, I., Islam, A., Ross, I., Li, S.: Tracking endocardial motion via multiple model filtering. *Biomedical Engineering, IEEE Transactions on* **57**(8) (2010) 2001–2010
4. Ben Ayed, I., Punithakumar, K., Li, S., Islam, A., Chong, J.: Left ventricle segmentation via graph cut distribution matching. in: *Medical Image Computing and Computer-Assisted Intervention—MICCAI 2009* (2009) 901–909
5. Cousty, J., Najman, L., Couprie, M., Clément-Guinaudeau, S., Goissen, T., Garot, J.: Segmentation of 4D cardiac MRI: Automated method based on spatio-temporal watershed cuts. *Image and Vision Computing* **28**(8) (2010) 1229–1243
6. Cocosco, C., Niessen, W., Netsch, T., Vonken, E., Lund, G., Stork, A., Viergever, M.: Automatic image-driven segmentation of the ventricles in cardiac cine MRI. *Journal of Magnetic Resonance Imaging* **28**(2) (2008) 366–374
7. Pednekar, A., Kurkure, U., Muthupillai, R., Flamm, S., Kakadiaris, I.: Automated left ventricular segmentation in cardiac MRI. *Biomedical Engineering, IEEE Transactions on* **53**(7) (2006) 1425–1428
8. Kurkure, U., Pednekar, A., Muthupillai, R., Flamm, S., Kakadiaris, I.: Localization and segmentation of left ventricle in cardiac cine-MR images. *Biomedical Engineering, IEEE Transactions on* **56**(5) (2009) 1360–1370
9. Kass, M., Witkin, A., Terzopoulos, D.: Snakes: Active contour models. *International journal of computer vision* **1**(4) (1988) 321–331
10. Paragios, N.: A level set approach for shape-driven segmentation and tracking of the left ventricle. *Medical Imaging, IEEE Transactions on* **22**(6) (2003) 773–776
11. Ben Ayed, I., Li, S., Ross, I.: Embedding overlap priors in variational left ventricle tracking. *Medical Imaging, IEEE Transactions on* **28**(12) (2009) 1902–1913
12. Wang, Y., Jia, Y.: Segmentation of the left ventricle from cardiac MR images based on degenerated minimal surface diffusion and shape priors. In: *Pattern Recognition, 2006. ICPR 2006. 18th International Conference on*. Volume 4., IEEE (2006) 671–674

13. Liang, J., Ding, G., Wu, Y.: Segmentation of the left ventricle from cardiac MR images based on radial GVF snake. In: BioMedical Engineering and Informatics, 2008. BMEI 2008. International Conference on. Volume 2., IEEE (2008) 238–242
14. Cootes, T.F., Taylor, C.J., Cooper, D.H., Graham, J., et al.: Active shape models-their training and application. Computer vision and image understanding **61**(1) (1995) 38–59
15. Cootes, T.F., Edwards, G.J., Taylor, C.J.: Active appearance models. Pattern Analysis and Machine Intelligence, IEEE Transactions on **23**(6) (2001) 681–685
16. Zhang, H., Wahle, A., Johnson, R.K., Scholz, T.D., Sonka, M.: 4-d cardiac mr image analysis: left and right ventricular morphology and function. Medical Imaging, IEEE Transactions on **29**(2) (2010) 350–364
17. Carneiro, G., Nascimento, J., Freitas, A.: The segmentation of the left ventricle of the heart from ultrasound data using deep learning architectures and derivative-based search methods. Image Processing, IEEE Transactions on **21**(3) (2012) 968–982
18. Petitjean, C., Dacher, J.: A review of segmentation methods in short axis cardiac MR images. Medical Image Analysis **15**(2) (2011) 169–184
19. Cohen, L.: On active contour models and balloons. CVGIP: Image understanding **53**(2) (1991) 211–218
20. Ray, N., Acton, S.: Motion gradient vector flow: An external force for tracking rolling leukocytes with shape and size constrained active contours. Medical Imaging, IEEE Transactions on **23**(12) (2004) 1466–1478
21. Xu, C., Prince, J.: Snakes, shapes, and gradient vector flow. Image Processing, IEEE Transactions on **7**(3) (1998) 359–369
22. Li, B., Acton, S.: Active contour external force using vector field convolution for image segmentation. Image Processing, IEEE Transactions on **16**(8) (2007) 2096–2106
23. Xie, X., Mirmehdi, M.: MAC: Magnetostatic active contour model. Pattern Analysis and Machine Intelligence, IEEE Transactions on **30**(4) (2008) 632–646
24. Caselles, V., Kimmel, R., Sapiro, G.: Geodesic active contours. International Journal of Computer Vision **22**(1) (1997) 61–79
25. Zhang, K., Zhang, L., Song, H., Zhou, W.: Active contours with selective local or global segmentation: A new formulation and level set method. Image and Vision Computing **28**(4) (2010) 668–676
26. Chan, T., Vese, L.: Active contours without edges. Image Processing, IEEE Transactions on **10**(2) (2001) 266–277
27. Li, C., Kao, C., Gore, J., Ding, Z.: Minimization of region-scalable fitting energy for image segmentation. Image Processing, IEEE Transactions on **17**(10) (2008) 1940–1949
28. Tang, J.: A multi-direction GVF snake for the segmentation of skin cancer images. Pattern Recognition **42**(6) (2009) 1172–1179
29. Mishra, A., Fieguth, P., Clausi, D.: Decoupled active contour (dac) for boundary detection. Pattern Analysis and Machine Intelligence, IEEE Transactions on **33**(2) (2011) 310–324
30. Cheng, J., Foo, S.: Dynamic directional gradient vector flow for snakes. Image Processing, IEEE Transactions on **15**(6) (2006) 1563–1571
31. Wu, Y., Jia, Y., Wang, Y.: Adaptive diffusion flow for parametric active contours. In: 20th International Conference on Pattern Recognition, ICPR 2010, IEEE (2010) 2788–2791
32. Xu, C., Prince, J.: Generalized gradient vector flow external forces for active contours1. Signal Processing **71**(2) (1998) 131–139
33. Lu, S., Wang, Y.: Gradient vector flow over manifold for active contours. In: Proceedings of the 9th Asian conference on Computer vision, ACCV 2009, Springer-Verlag (2010) 147–156
34. Ranganath, S.: Contour extraction from cardiac MRI studies using snakes. Medical Imaging, IEEE Transactions on **14**(2) (1995) 328–338
35. Makowski, P., Sørensen, T., Therkildsen, S., Materka, A., Stødkilde-Jørgensen, H., Pedersen, E.: Two-phase active contour method for semiautomatic segmentation of the heart and blood vessels from MRI images for 3D visualization. Computerized Medical Imaging and Graphics **26**(1) (2002) 9–17

36. Hautvast, G., Lobregt, S., Breeuwer, M., Gerritsen, F.: Automatic contour propagation in cine cardiac magnetic resonance images. *Medical Imaging, IEEE Transactions on* **25**(11) (2006) 1472–1482
37. Santarelli, M., Positano, V., Michelassi, C., Lombardi, M., Landini, L.: Automated cardiac MR image segmentation: theory and measurement evaluation. *Medical engineering & physics* **25**(2) (2003) 149–159
38. Lee, H., Codella, N., Cham, M., Weinsaft, J., Wang, Y.: Automatic left ventricle segmentation using iterative thresholding and an active contour model with adaptation on short-axis cardiac MRI. *Biomedical Engineering, IEEE Transactions on* **57**(4) (2010) 905–913
39. Nguyen, D., Masterson, K., Vallée, J.: Comparative evaluation of active contour model extensions for automated cardiac MR image segmentation by regional error assessment. *Magnetic Resonance Materials in Physics, Biology and Medicine* **20**(2) (2007) 69–82
40. Paragios, N.: A variational approach for the segmentation of the left ventricle in cardiac image analysis. *International Journal of Computer Vision* **50**(3) (2002) 345–362
41. Folkesson, J., Samset, E., Kwong, R., Westin, C.: Unifying statistical classification and geodesic active regions for segmentation of cardiac MRI. *Information Technology in Biomedicine, IEEE Transactions on* **12**(3) (2008) 328–334
42. Alessandrini, M., Dietenbeck, T., Basset, O., Friboulet, D., Bernard, O.: Using a geometric formulation of annular-like shape priors for constraining variational level-sets. *Pattern Recognition Letters* **32**(9) (2011) 1240–1249
43. Pluemptiwiriyawej, C., Moura, J., Wu, Y., Ho, C.: Stacs: New active contour scheme for cardiac mr image segmentation. *Medical Imaging, IEEE Transactions on* **24**(5) (2005) 593–603
44. Chen, T., Babb, J., Kellman, P., Axel, L., Kim, D.: Semiautomated segmentation of myocardial contours for fast strain analysis in cine displacement-encoded MRI. *Medical Imaging, IEEE Transactions on* **27**(8) (2008) 1084–1094
45. Lynch, M., Ghita, O., Whelan, P.: Left-ventricle myocardium segmentation using a coupled level-set with a priori knowledge. *Computerized Medical Imaging and Graphics* **30**(4) (2006) 255–262
46. Lynch, M., Ghita, O., Whelan, P.: Segmentation of the left ventricle of the heart in 3-D+ t MRI data using an optimized nonrigid temporal model. *Medical Imaging, IEEE Transactions on* **27**(2) (2008) 195–203
47. Punithakumar, K., Ben Ayed, I., Ross, I., Islam, A., Chong, J., Li, S.: Detection of left ventricular motion abnormality via information measures and bayesian filtering. *Information Technology in Biomedicine, IEEE Transactions on* **14**(4) (2010) 1106–1113
48. Osher, S., Sethian, J.: Fronts propagating with curvature-dependent speed: algorithms based on hamilton-jacobi formulations. *Journal of computational physics* **79**(1) (1988) 12–49
49. Zhu, Y., Papademetris, X., Sinusas, A., Duncan, J.: Segmentation of the left ventricle from cardiac MR images using a subject-specific dynamical model. *Medical Imaging, IEEE Transactions on* **29**(3) (2010) 669–687
50. Jolly, M.: Automatic segmentation of the left ventricle in cardiac MR and CT images. *International Journal of Computer Vision* **70**(2) (2006) 151–163
51. Duta, N., Jain, A.K., Dubuisson-Jolly, M.P.: Learning 2d shape models. In: *Computer Vision and Pattern Recognition, 1999. IEEE Computer Society Conference on. Volume 2.*, IEEE (1999)
52. Lorenzo-Valdés, M., Sanchez-Ortiz, G., Elkington, A., Mohiaddin, R., Rueckert, D., et al.: Segmentation of 4d cardiac mr images using a probabilistic atlas and the em algorithm. *Medical image analysis* **8**(3) (2004) 255–265
53. Mitchell, S.C., Lelieveldt, B.P.F., Van Der Geest, R.J., Bosch, H.G., Reiver, J., Sonka, M.: Multistage hybrid active appearance model matching: segmentation of left and right ventricles in cardiac mr images. *Medical Imaging, IEEE Transactions on* **20**(5) (2001) 415–423
54. Zambal, S., Hladuvka, J., Bühler, K.: Improving segmentation of the left ventricle using a two-component statistical model. *Medical Image Computing and Computer-Assisted Intervention—MICCAI 2006* (2006) 151–158

55. Wang, Y., Jia, Y.: Segmentation of the left ventricle from MR images via snake models incorporating shape similarities. In: *Image Processing, 2006 IEEE International Conference on, IEEE* (2006) 213–216
56. Wang, Y., Jia, Y.: External force for active contours: Gradient vector convolution. *PRICAI 2008: Trends in Artificial Intelligence* (2008) 466–472
57. Radau, P., Lu, Y., Connelly, K., Paul, G., Dick, A., Wright, G.: Evaluation framework for algorithms segmenting short axis cardiac mri. the midas journal—cardiac mr left ventricle segmentation challenge, 2009. [Online]. Available: <http://hdl.handle.net/10380/3070> (2009)
58. Yu, Z., Bajaj, C.L.: Normalized gradient vector diffusion and image segmentation. In: *Proceedings of the 7th European Conference on Computer Vision-Part III. ECCV '02* (2002) 517–530
59. Hou, Z., Han, C.: Force field analysis snake: an improved parametric active contour model. *Pattern Recognition Letters* **26**(5) (2005) 513–526
60. Rodtook, A., Makhanov, S.S.: Continuous force field analysis for generalized gradient vector flow field. *Pattern Recognition* **43** (October 2010) 3522–3538
61. Sum, K., Cheung, P.: Boundary vector field for parametric active contours. *Pattern Recognition* **40**(6) (2007) 1635–1645
62. Jifeng, N., Chengke, W., Shigang, L., Shuqin, Y.: NGVF: An improved external force field for active contour model. *Pattern Recognition Letters* **28**(1) (2007) 58–63
63. Wang, Y., Jia, Y., Liu, L.: Harmonic gradient vector flow external force for snake model. *Electronics Letters* **44**(2) (2008) 105–106
64. Li, C., Liu, J., Fox, M.: Segmentation of external force field for automatic initialization and splitting of snakes. *Pattern recognition* **38**(11) (2005) 1947–1960
65. Xie, X., Mirmehdi, M.: RAGS: Region-aided geometric snake. *Image Processing, IEEE Transactions on* **13**(5) (2004) 640–652
66. Zhu, G., Zhang, S., Zeng, Q., Wang, C.: Gradient vector flow active contours with prior directional information. *Pattern Recognition Letters* **31**(9) (2010) 845–856
67. Kovacs, A., Sziranyi, T.: Harris function based active contour external force for image segmentation. *Pattern Recognition Letters* **33**(9) (2012) 1180 – 1187
68. Wang, Y., Liang, J., Jia, Y.: On the critical point of gradient vector flow snake. In: *Proceedings of the 8th Asian conference on Computer vision-Volume Part II*, Springer-Verlag (2007) 754–763
69. Park, H., Chung, M.: External force of snake: virtual electric field. *Electronics Letters* **38**(24) (2002) 1500–1502
70. You, Y., Kaveh, M.: Fourth-order partial differential equations for noise removal. *Image Processing, IEEE Transactions on* **9**(10) (2000) 1723–1730
71. Otsu, N.: A threshold selection method from gray-level histograms. *Automatica* **11** (1975) 285–296
72. Ray, N., Acton, S., Ley, K.: Tracking leukocytes *in vivo* with shape and size constrained active contours. *Medical Imaging, IEEE Transactions on* **21**(10) (2002) 1222–1235
73. Mikic, I., Krucinski, S., Thomas, J.: Segmentation and tracking in echocardiographic sequences: Active contours guided by optical flow estimates. *Medical Imaging, IEEE Transactions on* **17**(2) (1998) 274–284